New approach in direct detection of Weakly Interacting Massive Particles

2016년

서강대학교 대학원
물 리 학 과
윤 국 현

New approach in direct detection of Weakly Interacting Massive Particles

지도교수 S. Scopel

이 논문을 이학박사 학위논문으로 제출함

2015년 1월 5일

서강대학교 대학원
물 리 학 과
윤 국 현

논 문 인 준 서

윤국현의 이학박사 학위논문을 인준함

2015 년 12월 14일

주심 임 채 호 ㊞

부심 김 원 태 ㊞

부심 박 정 혁 ㊞

부심 Stefano Scopel ㊞

부심 Carsten Rott ㊞

CONTENTS

LIST OF FIGURES

LIST OF TABLES

Abstract

After summarizing the observational evidence of Dark Matter in our Universe and the status of direct dark matter searches, in this Ph.D thesis we discuss how to generalize the standard direct detection analysis of Weakly Interacting Massive Particles(WIMPs) to a wider class of models. The standard direct detection analysis assumes coherent or spin–dependent WIMP-nucleus interactions from particle and nuclear physics and a thermalized WIMPs velocity distribution of our halo from astrophysics. On the other hand our generalized analysis extends the standard approach to virtually any WIMP-nucleus interaction allowed by Galilean invariance (implying possible explicit dependencies of the cross section on the transferred momentum and the WIMP incoming velocity) and to any velocity distribution. We show that when our generalized procedure is adopted several WIMP effective scenarios can be found for which the experimental excesses measured by DAMA, CDMS-Silicon and CRESST can be interpreted by a Dark Matter signal in agreement with constraints from other experiments.

CHAPTER I
INTRODUCTION

The most dominant constituent of matter in the universe which is called "*Dark Matter*" is non–luminous, non–baryonic and non–relativistic. The existence of the dark matter emerged from observation evidences and theoretical suggestions.

The first evidence from the virialized motion of the Coma cluster revealed that non–luminous matter is distributed. Furthermore, the dark matter which constitutes 23% of total density of the universe can be known by astrophysics observations, Cosmic Microwave Background Radiation(CMBR) and indirectly Big–Bang Nucleosynthesis(BBN).

The most popular candidate of the dark matter, "*Weakly Interacting Massive Particle*"(WIMP), is being measured the mass and cross–section by direct–detectors and indirect–detectors. Indeed, the Large Hadron Collider(LHC) wants to generate the WIMPs from the standard model particles.

A. History of the Universe

The Robertson–Walker (RW) metric can explain an evolution process of the universe and gives insights which the universe tells us. The RW metric is the outcome of homogeneous and isotropic universe which is written in (t, r, θ, ϕ) space as :

$$ds^2 = dt^2 - R^2(t)\left\{\frac{dr^2}{1-kr^2} + r^2 d\theta^2 + r^2 \sin^2\theta d\phi^2\right\}, \tag{I.1}$$

where the $R(t)$ is the cosmic scale factor and the k indicates a geometry of the universe such that chosen value within $+1$, 0 or -1 represents positive (closed), flat and negative (open) curvature (universe), respectively. Using the Einstein equation;

$$R_{\mu\nu} - \frac{1}{2}\mathcal{R}g_{\mu\nu} = 8\pi G T_{\mu\nu} + \Lambda g_{\mu\nu}, \tag{I.2}$$

where the $\mathcal{R}$ is the Ricci scalar, the $T_{\mu\nu}$ is the stress–energy tensor and the Λ is a cosmological constant which determines vacuum energy in the comoving frame. The 0–0 component of Einstein equation gives the Friedmann equation is written as :

$$\frac{\dot{R}^2}{R^2} + \frac{k}{R^2} = \frac{8\pi G}{3}\rho, \tag{I.3}$$

where ρ is energy density.

The Friedmann equation introducing the "*Hubble parameter*" $H \equiv \dot{R}/R$ can be recast as

$$\frac{k}{H^2R^2} = \frac{8\pi G\rho}{3H^2} - 1 \equiv \Omega - 1. \tag{I.4}$$

Here, $\Omega = \rho/\rho_c$, where the ρ_c is critical density which is equivalent to $3H^2/(8\pi G)$. The Hubble parameter in the present which is called "*Hubble constant*" is estimated by denoting with $H_0 \equiv 100h$ km/s/Mpc. A recent estimation[5] is $H_0 = 70 \pm 3$ km/s/Mpc.

The "*red shift*" z represents a stretching wavelength of photon due to the expanding universe. The stretching wavelength relates to a distance between source point and observing point with respect to cosmic scale factor such that :

$$\frac{R(t_0)}{R(t_1)} = \frac{\lambda_0}{\lambda_1} \equiv 1 + z, \tag{I.5}$$

where the times t_0 and t_1 conventionally represent the present and past, respectively. According to the measurable value z in the Eq(I.5), we can trace to the past universe with respect to the curvature k and the density ρ from the Hubble constant H_0.

Components of the universe is represented by the density ρ (or Ω). According to the stress–energy tensor and cosmological constant terms in the Eq(I.2), we can specify the evolution of the universe with respect to the radiation, matter and vacuum

energy dominant cases. The stress–energy tensor which is written in the form as $T^{\mu}_{\nu} = \mathrm{diag}\,(\rho, -p, -p, -p)$ represents the radiation as $\rho = 3p$, matter as $p = 0$ and the vacuum energy as $\rho = -p$ due to the fact that $T^{\mu\nu}{}_{;\nu} = 0$. The latest Plank data confirm that the total density of the universe is $\Omega \equiv \Omega_{\mathrm{Rad}} + \Omega_{\mathrm{M}} + \Omega_{\Lambda} = 1$, in the present we can neglect the radiation component due to the fact that the universe is cold enough. Reported values are $\Omega_{\mathrm{M}} = 0.3175$, $\Omega_{\Lambda} = 0.6825$ [6] and $\Omega_{\mathrm{M}} = 0.2735 \pm 0.027$, $\Omega_{\Lambda} = 0.727^{+0.030}_{-0.029}$[7].

B. Evidences from galaxy motion

In 1933 the proposition by Fritz Zwicky showed the non–luminous particles has to be imposed to explain the virialized motion of the Coma Cluster[8]. The viral theorem is that the relation between average value of kinetic energy $\langle T \rangle$ and potential energy $\langle V \rangle$ in a system is $2\langle T \rangle = -\langle V \rangle$. Due to the relation, F.Zwicky result[9] shows that the calculated mass by viral theorem is incompatible with observed luminous galaxies.

In 1970, the Vera C. Rubin and W. Kent Ford[10] observed rotation velocity of the Andromeda nebula. According to the Newtonian gravity field, the rotation velocity is proportional to $r^{-1/2}$. However, the Andromeda nebula does not follow the proportionality and so it should supplements non–luminous mass which is called dark halo such as Fig.10 (a) in [10] for explaining the observed data Fig.9 in [10]. The

Fig.I.1 shows the rotation curves which is represented by [1]. In [1], on the other hand, the modified Newtonian dynamics(MOND) which is modification of Newtonian force is no longer proportional to acceleration which was proposed by M. Milgrom[11] explains the flat rotation curves well. Even the MOND explains the rotational curves well, however, we will impose the dark halo due to other facts from astronomy observation.

On the other hand, the gravitational lensing effect and bullet cluster tell the dark matter existence. The gravitational lensing effect due to distribution of gravitation potential which can specify the mass of the photon trajectory. Especially, the bullet cluster gives not only the evidence, but also the property of dark matter which is collisionless due to a combination of the X–ray images and gravitational lensing.

C. Dark matter candidates

The dark matter is strange phenomenon which can not explained our knowledge in the standard model. There are many suggestions of dark matter such as neutrino, supersymmetric dark matter, Kaluza–Klein dark matter, Scalar singlet dark matter, Q–ball, mirror particles, axions, neutralinos, Strong Interacting Massive Particles (SIMP), CHArged Massive Particles (CHAMPs), etc. On the other hand when the Dark Matter is a thermal relic, which is one of the most popular scenarios, is has

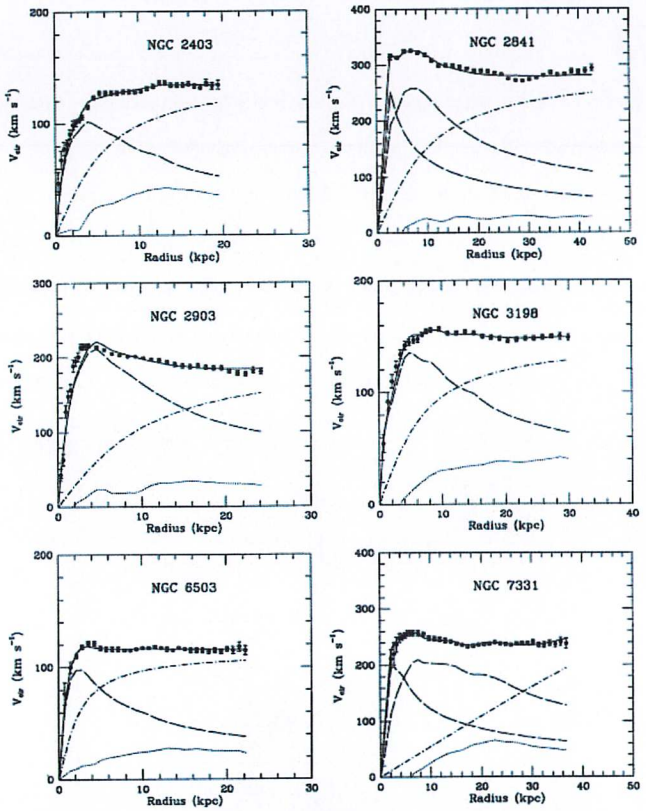

Figure I.1: Examples of rotation curve[1]; the dashed line is for visible components, the dotted line is for gas and the dash-dot line is for dark halo.

two bounds of the mass from cosmology, one is suggested by Cowsik–McClelland[12] m <few eV (Hot dark matter), the other is suggested by Lee–Weinberg[13] m >few GeV (Cold dark matter). The hot dark matter which can be suggested by standard model, however, is ruled out[14] by structure formation using N–body simulation and the abundant is not enough due to that $\Omega_\nu h^2 \leq 0.07$. The cold dark matter which is called Weakly Interacting Massive Particle (WIMP) is well motivated by following properties, stable, no charge, no colour, cold and relic abundance compatible to observations. The relic abundance ,which relates with freeze out due to Boltzmann equation in thermal equilibrium which is written as :

$$\frac{dn}{dt} + 3Hn = -\langle \sigma v \rangle \left(n^2 - n_{eq}^2 \right), \tag{I.6}$$

where n is number density, n_{eq} is number density in equilibrium, $\langle \sigma v \rangle$ is annihilation cross section, gives the cosmological density with respect to the annihilate particles which is approximately written as for WIMP :

$$\Omega_\chi h^2 \sim \langle \sigma v \rangle^{-1}, \tag{I.7}$$

where index χ is WIMPS.

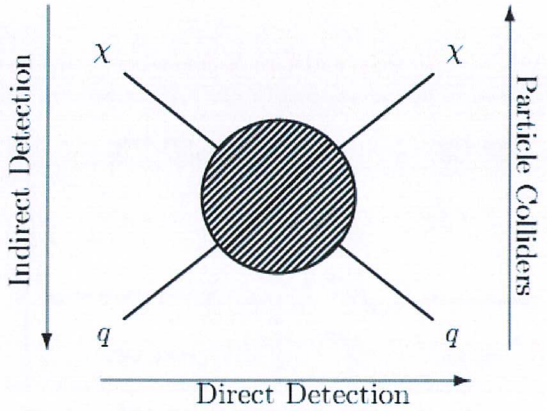

Figure I.2: Particle processes for WIMP searches

(1) WIMP searches

Typically, there are three ways to find the WIMP signals as shown Fig(I.2). The Particle Collider generates WIMP using the standard particle. The Large Hadron Collider first run at 8 TeV did not get discover any WIMP and is already running at 14 TeV.

The indirect detection detects the cosmic rays falling to the Earth. The cosmic rays is usually assumed by annihilated ones of WIMPs that is captured by the Sun. In the IceCube[15] and ANTARES[16] is running to find the WIMP candidate signals using neutrino which is annihilated by WIMP. The direct detection which is the main

subject of this thesis detects the WIMP directly. The running detectors, which we focus, and the strategy methods will be reviewed. The main advantage of the direct detection is that the directly scattered by targets in detectors reduce the uncertainty as like indirect detection.

CHAPTER II

ANALYSIS OF DIRECT DETECTION DATA

WIMP direct detection analysis can be calculated by 3 ingredients; experimental information, astrophysics and particle physics.

Event rate of WIMP in terms of energy can be calculated with[17]:

$$\frac{dR}{dE_R} = \frac{\rho_0}{m_N m_\chi} \epsilon(E_R) \int_0^\infty \int_{v_{\min}}^\infty \frac{f(\vec{v})}{v} \frac{d\sigma_{\chi N}}{dE'}(\vec{v}, E') G(E_R, E') \, d^3v dE'. \qquad \text{(II.1)}$$

In Eq(II.1), $\epsilon(E_R)$ is fraction of total exposure and effective exposure and the $G(E_R, E')$ is probability function which covers the uncertainty of detecting energy in detector are experiment information field. The $f(\vec{v})$ which is normalized WIMP velocity distribution around the Earth, and ρ_0 which is local WIMP density are astrophysics field. The last field, particle physics, is in the $\frac{d\sigma_{\chi N}}{dE'}$ which gives the cross section between WIMP and nucleus.

A. Standard analysis

The standard analysis means that the astrophysics and particle physics fields are assumed by simplest scenario. The simplest scenario assumes the astrophysics as Maxwellian and the particle physics as that is suggested by non–relativistic limit of extensions of the Standard Model as Supersymmetry or Extra dimensions. high energy effective field theory.

(1) Velocity distributions

The distribution of the WIMP in our Halo can be treated as collisionless gravitating system in stationary state. The density of the WIMPs $\rho(\vec{x})$, is integrated value of distribution function of WIMP in phase space $f(\vec{x}, \vec{v}, t)$ with respect to v and the time dependence term is negligible by the fact that $\dot{f}(\vec{x}, \vec{v}, t) = 0$ in collisionless case. The WIMPs are distributed by gravitational potential, ϕ, and it follows the Poisson equation $\nabla^2\phi = 4\pi G\rho$ where G is the gravitational constant. To find the distribution function from the density, convenient way is to shift the potential, ϕ, such as relative potential $\psi \equiv -\phi + \phi_0$ which ϕ_0 is a constant and will be chosen when ψ vanishing at the boundary of the system. The relative potential also follows the Poisson equation and we can define a relative energy such as $\epsilon = -E + \phi_0 = \psi - v^2/2$. The distribution function can be presented by relative energy, $f(\vec{x}, \vec{v}) = f(\epsilon)$, due to homogeneous

and isotropic properties come from the FRW universe model. Therefore, we can find the density with respect to distribution function

$$\rho(\vec{x}) = \int_0^{\psi} d\epsilon 4\pi f(\epsilon)\sqrt{2(\psi-\epsilon)} \tag{II.2}$$

then, by the Poisson equation, we can get

$$\frac{1}{\sqrt{8}\pi}\frac{d\rho(\psi)}{d\psi} = \int_0^{\psi} \frac{f(\epsilon)}{\sqrt{\psi-\epsilon}} d\epsilon. \tag{II.3}$$

Using the Abel integration equation, we can find solution of Eq(II.3) in distribution function such as

$$f(\epsilon) = \frac{1}{\sqrt{8}\pi^2}\frac{d}{d\epsilon}\int_0^{\epsilon}\frac{d\rho}{d\psi}\frac{d\psi}{\sqrt{\epsilon-\psi}}. \tag{II.4}$$

The density of isothermal sphere model which $\rho(r) = \rho_0 r_0^2/r^{-2}$ can be written with variable ψ as

$$\rho(\psi) = \rho_0 e^{\frac{\psi}{\sigma^2}}, \tag{II.5}$$

where ρ_0 is local density around the Earth(ref), r_0 is the distance between the Earth and the Galactic center and the σ is a constant. Using Eq(II.4), the distribution function is

$$f(v) = \begin{cases} \frac{1}{N_{\rm esc}}\left(\frac{3}{2\pi\sigma_v^2}\right)^{\frac{3}{2}} e^{-\frac{3\vec{v}^2}{2\sigma_v^2}}, & \text{for } |\vec{v}| \le v_{\rm esc} \\ 0, & \text{otherwise} \end{cases}, \tag{II.6}$$

where the σ_v is WIMP root–mean–square (rms) velocity and the $v_{\rm esc}$ is WIMP escape velocity. Moreover, the $N_{\rm esc}$ is normalization factor which is written as

$$N_{\rm esc} = \mathrm{erf}(z) - \frac{2}{\sqrt{\pi}} z e^{-z^2}, \tag{II.7}$$

where $z \equiv v_{\rm esc}/v_0$. The $\vec{v}_0$ is estimated through vector addition by peculiar velocity of the Sun, $\vec{v}_s$, galactic rotation velocity, $\vec{v}_r$, and the Earth velocity relative to the Sun $\vec{v}_e$. The velocities are usually assumed by $\vec{v}_s = (9, 12, 7)$km/s, $\vec{v}_r = (0, 230, 0)$km/s, the Earth mean orbital velocity in orbital direction, $v_e = 29.8$km/s and $v_{\rm esc} = 550$km/s[18]. Besides, rotation in orbital direction and escape velocity are suggested that $v_r = 243 \pm 20$km/s[19], 222 ± 20km/s[20] and 228 ± 19km/s[21], and $580\text{km/s} \le v_{\rm esc} \le 625$km/s[22], respectively. The WIMP root–mean–square velocity is determined by hydrostatic equilibrium which the net force between gravitational attraction and repulsive force of WIMP pressure in spherical symmetry. According this, the root–mean–square relates to rotational velocity such that $\sigma_v = \sqrt{3/2}v_0$. On the other hand, according to the bottom–up cold dark matter scenario of structure formation, the remnants of the merger history of our galaxy embroider non–thermal components in our galaxy such as "*tidal streams*". Hence, a tidal stream is spatially confined to one direction which the functional form of the velocity distribution neglecting dispersion is $f(\vec{v}) = \delta(\vec{v} - \vec{v}_{\rm stream})$. One of examples of tidal streams,

the Sagittarius stream[23], is associated with the on–going tidal disruption of the Sagittarius dwarf galaxy. It suggests that speed along orthogonal direction to the Galactic plane relative to the Sun is $|\vec{v}_{\rm stream}| \sim 350$km/s and local density is 10%. Moreover, the Sloan Digital Sky Survey(SDSS) which is a tool for the identification of Galactic substructure suggests candidates of tidal streams such as Monoceros and Orphan streams[24, 25]. Another non–thermal component is "*Debris flow*"[26, 27] according to "N-body" simulation. Main difference from the tidal streams is that the debris is not the remnants of the merger history but is outcome material of the many small structures tidal stripping when they are eaten up by the Milky way. The outcome material in early times has enough time to spatially mix to become usual Maxwellian, while the debris is formed by outcome material from disrupted small structures in later times. The functional form of the debris with neglecting dispersion, $f(\vec{v}) = \delta(|\vec{v}| - v_{\rm debris})$, implies that even though the outcome material is not completely thermalized, the spherical symmetry of the galactic gravitation potential is descent.

In addition, velocity distribution is estimated by the highest resolution numerical simulation: Via Lactea II(VL2)[28] and GHALO[29] which are hierarchical evolution from $z = 104.3$ and $z = 58$ to the present, respectively. A simple way to parametrize

of N-body simulation to halo density[30] is:

$$\rho(r) = \frac{\rho_0}{(r/R)^\gamma \left[1 + (r/R)^\alpha\right]^{(\beta-\gamma)/\alpha}}, \tag{II.8}$$

where the R is characteristic scale lengths, the (α, β, γ) is parameters to determine profile models such as Kra[31] : (2,3,0.4), $R = 10$kpc, Moore[32] : (1.5,3.0,1.5), $R = 28$kpc, NFW[33] : (1,3,1), $R = 20.0$kpc and modified Isothermal[34] : (2,2,0), $R = 3.5$kpc. Also, the ρ_0 is the density of spherical dark matter halo with flat core.

(2) WIMP-nucleus cross section

According to the interaction between WIMP and target nucleus, the rest target is recoiled by scattering of WIMP off nuclei such as process, $\chi + {\rm N}_{\rm rest} \to \chi + {\rm N}_{\rm recoil}$. The direct detector detects the recoil energy and its rate. Indeed relation between WIMP velocity and recoil energy by classical mechanics. Center of mass frame in fig.(II.1) recast nuclear recoil energy E_R which is represented by $\vec{v}_{\rm N}$ as :

$$E_R = \frac{1}{2} m_\chi v^2 \times \frac{4 m_\chi m_{\rm N}}{(m_\chi + m_{\rm N})^2} \times \frac{1 + \cos\theta}{2}, \tag{II.9}$$

where the scattering angle θ is given by the unknown out–going WIMP velocity. As the relation, conventionally, $v_{\rm min}$ which gives the maximum recoil energy $E_R^{\rm max}$ is

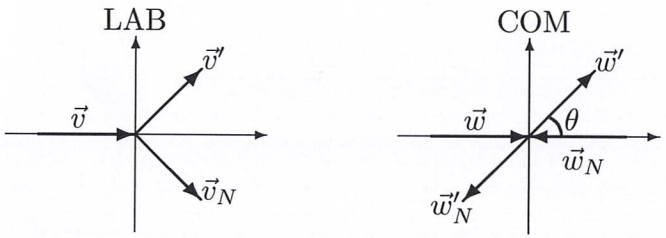

Figure II.1: Scattering diagram in Lab frame and center of mass(COM) frame.

defined as

$$v_{\min} = \sqrt{\frac{m_N E_R}{2\mu^2_{\chi,\text{nucleus}}}} \tag{II.10}$$

In other word, when the recoil energy fixed, possible WIMP velocity is $v_{\min}$ to infinity. When we neglect the experiment uncertainties, in a simple scattering, an isotropic WIMP–nucleus cross section is written as :

$$\frac{d\sigma_{\chi N}}{dE_R} = \frac{\sigma_{\chi N}(E_R)}{E_R^{\max}}. \tag{II.11}$$

Here, the $\sigma_{\chi N}(E_R)$ is factorized to $\sigma_0 F^2(qR_N)$, where σ_0 is point–like cross section and $F(qR_N)$ is form factor where the transferred momentum, $q = \sqrt{2m_N E_R}$. The point–like cross section depends on particular dark matter candidates which the most popular models are scalar and axial–vector coupling. On the other hand, the form

factor takes into account the finite radius of the nucleus R_N due to wavelength of momentum transfer in WIMP–nucleus collision. For instance, when the target nucleus is small enough, the point–like cross section is valid, while in the sizable nuclear target case there is loss of coherence.

(a) SI coupling

The SI cross section is presented by the effective interaction term $(\bar{\chi}\chi)(\bar{q}q)$. In this case, the point–like cross section is written as :

$$\sigma_{0,\text{SI}} = \frac{4}{\pi}\mu^2_{\chi,\text{nucleus}}\left[Zf_p + (A-Z)f_n\right]^2 = \sigma_{\text{nucleon}}\frac{\mu^2_{\chi,\text{nucleus}}}{\mu^2_{\chi,\text{nucleon}}}\frac{\left[Zf_p + (A-Z)\,f_n\right]^2}{f_p^2}, \tag{II.12}$$

where the σ_{nucleon} is WIMP nucleon(proton or neutron) cross section, Z and $A-Z$ are the number of proton and neutron, respectively, and $\mu^2_{\chi,\text{nucleus}}$ and $\mu^2_{\chi,\text{nucleon}}$ are WIMP–nucleus and nucleon reduced mass, respectively. In addition, f_p and f_n are effective couplings to proton and neutron which are usually assumed equal, $f_p \simeq f_n$. The form factor for SI is calculated by the Fourier transformation of normalized nuclear mass density $\rho(\vec{r})$ such that

$$F(q) = \int \rho(\vec{r}) e^{i\vec{q}\cdot\vec{r}} d^3r. \tag{II.13}$$

The Helm parametrization[35] assume the $\rho(\vec{r})$ as rigid sphere smeared out by skin factor s such that :

$$\rho(\vec{r}) = \int d^3\vec{r}\,'\rho_0(\vec{r}\,')\rho_1(\vec{r}-\vec{r}\,'), \tag{II.14}$$

where the $\rho_0(\vec{r})$ is constant when $r^2 \leq R_0^2 = R_N^2 - 5s^2$ and otherwise is zero where R_0 is called effective nuclear radius. Then the $\rho_1(\vec{r}) = \exp\left[-\frac{1}{2}\left(\frac{r}{s}\right)^2\right]$ where the skin factor s is usually assumed as 0.9fm [18] which is improved by a matching between Helm and Fermi density distribution[36]. Therefore, the Helm form factor is

$$F(q) = \frac{3j_1(qR_0)}{qR_0}e^{-\frac{1}{2}q^2s^2}, \tag{II.15}$$

where the $j_1(x)$ is the 1^{st} order Bessel function and the nuclear radius is assumed as $R_N \sim 1.2A^{1/3}$fm.

(b) SD coupling

The SI interaction depends on the nuclear size. However, the interaction between WIMP and spin of the nucleus target which effective interaction is $(\bar{\chi}\gamma_\mu\gamma_5\chi)\,(\bar{q}\gamma^\mu\gamma_5 q)$, SD scattering, comes up only in the unpaired proton or neutron. The point–like cross section about the SD interaction is written as :

$$\sigma_{0,SD} = \frac{32\mu^2_{\chi,\text{nucleus}}}{\pi}G_F^2 J\,(J+1)\,\Lambda^2, \tag{II.16}$$

where G_F is the Fermi constant, J is the spin of the nucleus and

$$\Lambda = \frac{1}{J}\left(a_p\langle S_p\rangle + a_n\langle S_n\rangle\right).$$

Here, the a_p and a_n are effective couplings to proton and neutron, respectively, and the $\langle S_p\rangle$ and $\langle S_n\rangle$ are the expected values of spin for proton and neutron, respectively. The SD form factor depends on the spin structure function which is defined as $S(q) = a_0^2S_{00}(q) + a_1^2S_{11}(q) + a_0a_1S_{10}(q)$ in terms of isoscalar($a_0 = a_p + a_n$) and isovector ($a_1 = a_p - a_n$) which are computed using the shell models[37], numerically. However, according to the thin shell distribution, approximately, the form factor is simply assumed as :

$$F^2(q) = e^{-\frac{1}{3}(qR_0)^2}. \tag{II.17}$$

Also, the expected values of spin[38] in the zero momentum limit can be found by the following relations with the structure functions :

$$\langle S_p\rangle^2 = (S_{00} + S_{11} + S_{01})/4, \quad \langle S_n\rangle^2 = (S_{00} + S_{11} - S_{01})/4,$$
$$\langle S_p\rangle\langle S_n\rangle = (S_{00} - S_{11})/4.$$

The total cross section is the sum of both spin independent and dependent interaction. However, the spin dependent interaction is negligible because i) the expected

Yes, but bounds on σ_{SI} are also much more stringent than σ_{SD}

value of the spin which has a tendency to cancel for a large number of nucleons is not to be compared with spin independent interaction which is proportional to A^2 and ii) nuclei with an even number of nucleons have very small or vanishing spin–dependent cross sections.

B. Direct detectors

The WIMP direct detection is well motivated to find candidate of GeV–scale WIMP signals with respect to keV–scale nuclear recoil energy. In the present, running experiments are DAMA[2], KIMS[39], Xenon 10[40], LUX[41], PICO-2L, PICASSO, COUPP, SIMPLE, CRESST, Super CDMS, CDMS–Si, CDMS–Ge, CoGeNT, CDMSlite and so on. The direct detections measure one or combination of two of three types of signals which are ionization, scintillation and heat–phonon. The ionization signal is caused by the escape electron from the nucleus when WIMP scattering gives enough energy. The scintillation signal is caused when the exited electron state due to WIMP scattering returns to the stable state by emitting a photon. The heat–phonon signal is caused by temperature vibration due to the vibrating crystal lattice by WIMP scattering. When the ionization or scintillation signals are detected, corresponding energy is electron equivalent energy, E_{ee}(keV$_{ee}$ unit) while the signals is happened by interaction between nucleus and WIMP which is related with nuclear recoil energy

reference +XENON100 +XMASS

E_R(keV$_{nr}$ unit). The electron equivalent energy is reduced compared to the nuclear recoil energy by quenching effect and the relation is determined by $E_{ee} = Q(E_R)E_R$ where the $Q(E_R)$ is quenching factor. On the other hand, in the heat–phonon signals, there are no quenched signals, in other words, the electron equivalent and nuclear recoil energy are same[42, 43]. The effective efficiency reduces the total exposure due to cuts applied to lower external and internal backgrounds.

Each measurement has advantage and disadvantage, however, development goal of the detector is to reduce backgrounds and extend to low threshold energy. Because, in the standard analysis which is explained before, expected rate of the WIMP in direct detection is exponentially decreasing due to the form factor, hence it concentrates in low energy.

We will review experimental informations which is concerned in this thesis in the following. In particular, the DAMA experiment is explained more than others because it detects a potential WIMP signal using a method (annual modulation) different from other experiments.

zero background experiments vs. "high-rate" annual modulation

DAMA is the longest running experiment which collects scintillating signal using NaI(Tl) crystal during 14 years (7 years DAMA/LIBRA + 7 years DAMA/NaI) with cumulative exposure 1.33 ton×yr[2]. Especially, DAMA gives annual modulation data which can discriminate the background. In theory, the signal can be decomposed in unmodulated and modulated parts due to the Earth revolution around the Sun such

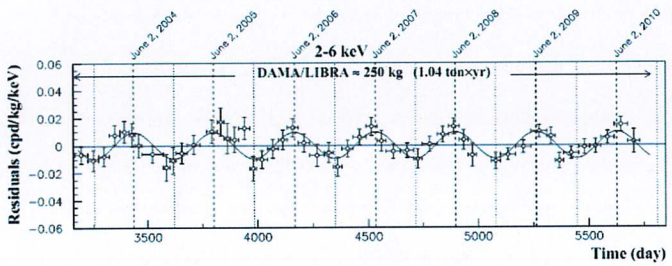

Figure II.2: Experimental residual rate of the single-hit scintillation events measured by DAMA/LIBRA-phase1 in the (2-6) keV$_{ee}$energy interval as a function of the time (error bar). The superimposed curve is fitting with $S_m \cos\omega\,(t-t_0)$. The dashed lines correspond to the maximum signal and the dotted lines correspond to the minimum[2]

that :

$$S = S_0 + S_m \cos\omega\,(t-t_0)\,, \tag{II.18}$$

where the S_0 is unmodulated signal, the S_m is modulate amplitude, the $\omega = 2\pi/T$ here the $T = 365.25$ days and the $t_0 = 152.5$ day (June 2nd) which gives the maximum signal as shown in Fig(II.2). The modulated data such as Fig(II.2), sinusoidal assumption well fit from Eq(II.18) with the modulation amplitude $S_m = 0.0112 \pm 0.0012$cpd/kg/keV corresponding to 9.2σ C.L., when unmodulate part is neglected. Important data for direct detection analysis is the event rate with respect to the recoil energy or electron equivalent energy. The Fig(II.3) shows that the residual rate to electron equivalent energy in cpd/kg/keV unit. To interpret the

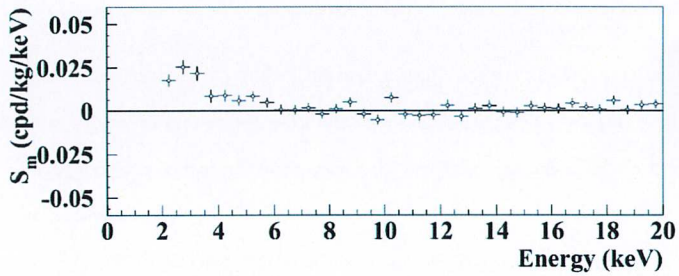

Figure II.3: Annual modulate event rate in electron equivalent energy. The energy bin is 0.5 keV[2]

DAMA event with expected rate from Eq(II.1), we should know effective exposure and the quenching factors for sodium and iodine. In DAMA case, the rate is already normalized to a day and the residual rate has already reduced backgrounds by using single–hit scintillation events. Reported values of the quenching factors for sodium and iodine in [44] are $Q_{\rm Na} = 0.3 \pm 0.01$ and $Q_{\rm I} = 0.09 \pm 0.01$ in energy range 2 to 30 keV$_{ee}$and in [45] are $Q_{\rm Na} = 0.4 \pm 0.2$ in energy range 2 to 40 keV$_{ee}$and $Q_{\rm I} = 0.05 \pm 0.02$ in energy range 2 to 20 keV$_{ee}$. Also, to consider the electron equivalent energy uncertainty such the $G(E,E')$ in Eq(II.1), the function is assumed by Gaussian probability distribution function which can be written as:

$$G(E,E') = \frac{1}{\sqrt{2\pi}\sigma_{\rm res}(E')} \exp\left[-\frac{(E-E')^2}{2\sigma_{\rm res}(E')^2}\right], \tag{II.19}$$

where dispersion $\sigma_{\rm res}(E')$ (Energy resolution) depends on experiment which usual form is $\sigma_{\rm res}(E') = a\sqrt{E'} + bE'$. The DAMA case, the values are $a = 0.448$ and $b = 0.0091$[46]. Indeed, as Fig(II.3), the modulating signals are in the $2-4$ keV$_{ee}$range.

Xenon 10 collects combination of ionization electron(S2) and scintillation photon(S1) signals with Xenon liquid. Result[40] presents the S2 yields which counts electrons. The WIMP candidate events are presented in recoil energy in 1.4–10 keV$_{\rm nr}$range which is corresponding to the number of electrons(Fig2 in [40]). The relation between recoil energy and the number of electron can be found in [47, 48] which is written as (the parameters are defined in [47])

$$\mathcal{Q}_y \equiv \frac{n_e}{E_R} = \frac{1}{\xi}\ln(1+\xi)\frac{f_n(k)/\epsilon}{1+N_{ex}/N_i}. \tag{II.20}$$

The Xenon 10 result shows with 15 kg–days after background discrimination and the total number of ~~event~~ events are 23. The energy resolution is used Poisson distribution which relation is $\sqrt{N}$ for N events in recoil energy unit such as $\sigma_{\rm res}(E_R) = (\mathcal{Q}_y E_R)^{-1/2}$.

LUX collects same signals with Xenon 10 during 85.3 days with a fiducial volume of 118 kg. In first result[41], interest range is 2–30 photoelectron(phe). However, it focuses on the $S1$ yield of Xenon liquid. In calculation we adopt null signal while it can be found the exact signals in Fig4 in [41]. The efficiency is adopted from Fig9 in [41]. The relation between nuclear recoil energy and photoelectron is generally

written as[49]

$$\nu(E_R) = E_R \times \mathcal{L}_{eff}(E_R) \times \frac{S_{\rm nr}}{S_{\rm ee}} \times L_y. \tag{II.21}$$

For LUX the estimation of the normalization light yield is $L_y = 8.8$phe/keV$_{ee}$for 122 keV γ–rays at zero field, so the scintillating quenching factors for electronic $S_{\rm ee}$ and for nuclear recoil $S_{\rm nr}$ due to the electronic field are set to one. In addition, the $\mathcal{L}_{eff}(E_R)$ which is scintillation efficiency including the effect of the electric field is presented by Slide 25 in [50], so to estimate the S1 uncertainty we take the Gaussian distribution with energy resolution such as $\sigma(E) = \sqrt{n}\sigma_{\rm PMT}$, where the $\sigma_{\rm PMT} = 0.5$phe is finite average single photoelectron resolution. (It will be explain why $S1$ uncertainty is presented in LUX.)

Xenon 100 Experimental information for Xenon 100 is assumed by the two event scattering with Xenon at $S_1 = 3.3$PE, 3.8PE as shown Fig(2) in [51] in the experimental range $3\text{PE} \leq S_1 \leq 30\text{PE}$ for an 224.6kg–days with a fiducial volume of 34kg. Moreover, according to the Eq(II.21), we assumed from [52] as $L_y = 2.28$PE, $S_{\rm nr} = 0.95$, $S_{\rm ee} = 0.58$ and $\mathcal{L}_{eff}(E_R)$ is taken from Fig(1). The energy resolution is same procedure with LUX.

KIMS collects scintillating signal using CsI(Tl) crystal. The interested energy range is 2–4 keV$_{ee}$and it find null signal with total exposure of 24,524.3 kg–days[39]. The quenching factor of CsI(Tl) crystal depends on energy which is presented at Fig13

in[53]. The efficiency is presented at Fig1(a) in [39].

CoGeNT It gives also annual modulation data [54], while in this thesis we only consider both the total count rates scattering with Germanium and the background from Fig(23) of [55] rescaling them to the exposure of 1129 day[56](This reference presents the raw data) for fiducial volume 0.33kg in the signal range 0.5keV$_{ee}$< E_{ee} <2keV$_{ee}$. The quenching factor is given as $Q_{\rm Ge} = 0.2 \times E_R^{0.12}$ by [54] and the energy resolution is given as $\sigma_{\rm res}(E') = \sqrt{69.7^2 + 0.976(E'/{\rm eV})}$ in eV [57]

CDMS–Si Three events, scattering with silicon, are given at E_R =8.2keV$_{\rm nr}$, 9.5keV$_{\rm nr}$and 12.3keV$_{\rm nr}$in the energy range 7keV$_{\rm nr}$< E_R <100keV$_{\rm nr}$with exposures of 140.2kg–days[58], while we take 8keV$_{\rm nr}$< E_R <12.5keV$_{\rm nr}$to concentrate the excess. The efficiency is shown in Fig(1) in [58] energy resolution of silicon is assumed as $\sigma_{\rm res}(E) = \sqrt{0.293^2 + 0.056^2\,E}$ [59]. (The energy resolution of silicon has not been measured while [59] shows germanium energy resolution below 10keV$_{\rm nr}$.)

SuperCDMS SuperCDMS[60] is low–energy analysis in the energy range 1.6keV$_{\rm nr}$< E_R <10keV$_{\rm nr}$with Germanium target. There are 11 observed WIMP candidate from T2Z1, T2Z2, T5Z2 and T5Z3 detectors with the total exposures of 577kg–days. The efficiency is shown in Fig(1) in [60] and the energy resolution is same with silicon, $\sigma_{\rm res}(E) = \sqrt{0.293^2 + 0.056^2\,E}$ [59].

CDMS–Ge The result is presented by digital format about T1Z2, T1Z5, T2Z3 and T2Z5 detectors from [61]. In particular, in this thesis, we take the T1Z5 detector which the WIMP candidate event in recoil energy and exposures are given by [61], while the efficiency is taken from Fig(1) in [61] with the energy range 2keV$_{\rm nr}$< E_R <100keV$_{\rm nr}$. Moreover, the energy resolution is assumed as $\sigma_{\rm res}(E) = \sqrt{0.293^2 + 0.056^2\,E}$ [59].

CDMSlite The energy range is 0.170keV$_{ee}$< E_{ee} <7keV$_{ee}$, due to voltage–assisted, with 0.6kg of germanium during 10 live days. The WIMP event in the electron equivalent energy is given by Fig(1) in [62] while the quenching factor is adopted the CoGeNT factor. In this analysis, we take the energy resolution as $\sigma_{\rm res}$ = 14keV and the efficiency cut as $\xi_{\rm cut} = 0.985$ [62].

SIMPLE The SIMPLE experiment[63] uses superheated liquid droplets homogeneously distributed in a gel to search for transitions to the gas phase produced by WIMP scatterings. The nuclear targets are made of C_2ClF_5 (for the nuclear response function of chlorine, which is not available from [64, 65, 66], we have used a simple estimation outlined in Eq(III.9)). SIMPLE is a threshold detector, only sensitive to the minimal deposited energy E_{th} required to trigger the nucleations, and with E_{th} controlled by the pressure of the liquid. The probability that an energy deposition E_R on the target nucleus T nucleates a droplet is given by:

$$P_T(E_R) = 1 - \exp\left[-\alpha_T \frac{E_R - E_{th}}{E_{th}}\right], \qquad \text{(II.22)}$$

where α_T is determined by fitting calibrations with neutron sources. With an exposure of 6.71 kg day and E_{th}=7.8 SIMPLE observed 1 event, consistent to an expected background of 2.2. This can be converted to an upper bound of 3.16 events using the Feldman-Cousin method [3]. We use α_F=α_C=3.6.

CRESST We only focus on scatterings on Tungsten in $CaWO_4$. To this aim we select from [67] the 45 events (out of 67) in the W recoil bands of Figs. 7, 9 and 17 in the total energy range 10 keV_{nr}< E_R < 40keV_{nr}collected with an exposition of 730 kg day [1]. The background in the W band is dominated by lead recoils from ^{210}Po decays, which we model as in Eq(1) of Ref.[67]. When discussing $v_{\min}$ ranges and the self–consistency checks of we select the signal region 12 keVnr< E_R < 24 keVnr where we optimize the signal/background ratio getting 34 total events vs. a background of 7.4. As far as the energy resolution is concerned, we use the two measurements FWHM(E′=3.6 keVnr) = 0.3 keV and FWHM(E′= 64 keVnr) = 1.6 keVnr from [69] to fit the functional form $\sigma_{CRESST}(E')$ =-0.0442+0.0904$\sqrt{E'}$ in keVnr (FWHD=2.355×σ).

COUPP The COUPP experiment[70] searches for WIMPs using nucleations in a bubble chamber and is also a threshold detector. In the case of COUPP the target material is CF_3I. For each operating threshold used in COUPP the corresponding exposure, expected background, number of measured events and 95% C.L. upper bound

[1] After submission of the present manuscript new unpublished CRESST data have been presented in [68] that do not confirm the excess claimed in [67].

E_{th} (keV)	exposure (kg day)	backgrounds	events	95% C.L.
7.8	55.8	0.8	2	5.92
11	70	0.7	3	8.26
15.5	311.7	3	8	12.29

Table II.1: For each operating threshold used in COUPP we provide the corresponding exposure, expected background, number of measured events and 95% C.L. upper bound obtained with the Feldman-Cousin method [3] used in our analysis

obtained with the Feldman-Cousin method [3] used in our analysis are summarized in Table II.1. We adopt the nucleation probability (II.22) with α_F=α_C=0.15, while for iodine we assume P_I=1, corresponding to $\alpha_I \to \infty$ in (II.22).

PICASSO The Picasso experiment[4] is a bubble chamber using C_3F_8, operated with eight energy thresholds. For each of the latter we provide the corresponding upper bound on the number of events (normalized to events/kg/day) in Table II.2 (extracted from Fig. 5 of Ref.[4]). We use the nucleation probability of Eq.(II.22) with α_C=α_F=5.

PICO-2L The PICO-2L collaboration operated a C_3F_8 bubble chamber experiment with four energy thresholds. For each of them we provide the corresponding exposure, number of measured events and 95% C.L. upper bound (conservatively assuming zero background) used in our analysis in Table II.3. In particular we conservatively chose to use the raw data without the subtraction adopted in [71] which makes use of time correlations among measured events. We adopt the nucleation

E_{th} (keV)	95% C.L.
1.7	1.1
2.9	1.5
4.1	11
5.8	9
6.9	1.3
16.3	3.1
39	1.5
55	6

Table II.2: 95% C.L. upper bounds (extracted from Fig. 5 of Ref.[4]) for each operating threshold used in PICASSO.

E_{th} (keV)	exposure (kg day)	measured events	95% upper bound
3.2	74.8	9	16.77
4.4	16.8	0	3.09
6.1	82.2	3	8.25
8.1	37.8	0	3.09

Table II.3: For each operating threshold used in PICO-2L we provide the corresponding exposure, number of measured events and 95% C.L. upper bound (assuming zero background) used in our analysis.

probability (II.22) with α_F=α_C=0.15.

C. Direct detection analysis

In standard analysis with direct detection data, we adopt several assumptions as reviewed above. In this section, the Eq(II.24) will be explained in the view of direct detection data. In particular, the astrophysics term which gives the velocity distribution should be presented in modulation and unmodulation terms in local frame. Moreover, as above, event rate of LUX experiment should be presented in the S1 event.

(1) Velocity distribution

The velocity distribution equation Eq(II.6) is adapted to $\eta(v_{\min})$ which is defined as

$$\eta(v_{\min}) = \int_{v_{\min}}^{\infty} \frac{f(\vec{v})}{v} dv, \tag{II.23}$$

where $v = |\vec{v}|$. According to Eq(II.23), the event rate can be written as

$$\frac{dR}{dE'} = \frac{N_T \rho_0 \sigma_0}{2 m_\chi \mu^2_{\chi,\text{nucleus}}} \epsilon(E') \int_0^{\infty} \eta\left[v_{\min}(E_R)\right] G(E_R, E') F\left[q\left(E_R\right)\right]^2 dE_R, \tag{II.24}$$

where E' is the observed recoil energy and the N_T is the number of target nuclei per unit mass. Here, the ρ_0 is the WIMP local density.

The $\eta(v_{\min})$ for unmodulated maxwellian velocity distribution is

$$\eta(x_{\min}) = \frac{N_{\rm esc}}{\alpha}\left(\frac{3}{2\pi\omega^2}\right)^{\frac{1}{2}} \times \begin{cases} \xi\left(x_{\min}-\alpha, x_{\min}+\alpha\right) - 2\alpha e^{-z^2}, & x_{\min} < z-\alpha \\ \xi\left(x_{\min}-\alpha, z\right) - 2\alpha e^{-z^2}\left(z+\alpha-x_{\min}\right), & z-\alpha \le x_{\min} \le z+\alpha \\ 0, & x_{\min} > z+\alpha \end{cases}, \quad \text{(II.25)}$$

where the $x_{\min}$ and α are dimensionless variables which are defined as

add space

$$x_{\min} = \frac{3v_{\min}}{2v_0}, \alpha = \frac{3v_{\rm loc}}{2v_0}.$$

Here, the $v_{\rm loc}$ is the Earth velocity with respect to the Galactic center.

While, the $\xi(x,y)$ is defined as

$$\xi = \frac{\sqrt{\pi}}{2}\left[\mathrm{erf}(y) - \mathrm{erf}(x)\right], \quad \text{(II.26)}$$

where the $\mathrm{erf}(x)$ is error function which is presented as

$$\mathrm{erf}(x) = \frac{2}{\pi}\int_0^x e^{-y^2} dy.$$

The unmodulated $\eta\left(v_{\min}\right)$ does not consider revolution of the Earth, because the average velocity is only due to the Sun velocity. However, in the local frame, it includes an effect due to the revolution of the Earth which gives time–dependence. In particular, modulated data from DAMA experiment is the difference between the maximum and the minimum signals during a year. Due to the Earth revolution velocity with respect to time which can be written as [72]

clarify: around the sun (not daily rotation)

$$v_{\rm loc} \equiv |\vec{v}_{\rm loc}| \simeq 233.5 + 14.4\cos\left[\omega\left(t-t_0\right)\right] \mathrm{km/s}, \quad \text{(II.27)}$$

where $t_0 \simeq 125$ days, the $\eta(v_{\min})$ can be decomposed to

$t = 0 - 365$ days ?
$\omega = ?$

$$\eta(v_{\min}) \equiv \eta_0(v_{\min}) + \eta_1(v_{\min}, t) = \eta(v_{\min})|_{v_e=0} + \frac{\partial\eta(v_{\min})}{\partial\alpha}\Delta\alpha\cos\left[\omega\left(t-t_0\right)\right], \quad \text{(II.28)}$$

where the $\Delta\alpha = 14.4$ km/s. Moreover, η_1 can be determined by a fit to the time–dependence of the signal, or calculated by difference between 2nd June. and 2nd Dec. which is the maximum and the minimum, respectively.

t_0 ?

(2) Event rate in observed recoil energy

Eq(II.1) is presented in terms of nuclear recoil energy, thus we need to convert it into the electron–equivalent energy. Therefore it can be found by change of variable and

chain rule for energy integration ($1/Q$ is added). However, in LUX (and Xenon100 which is not introduced) experiment which the result is presented in terms of the S1 event, the event rate is calculated by[49] :

$$\frac{dR}{dS1} = \sum_{n=1}^{\infty} G(S1|n, \sqrt{n}\sigma_{\rm PMT}) \frac{dR}{dn} \zeta(S1), \tag{II.29}$$

where the $\zeta(S1)$ is the acceptance (0.5 is multiplied, additionally, for average discrimination due to quality cut for LUX[41]) and the dR/dn is event rate in number of photoelectrons which is written as:

$$\frac{dR}{dn} = \int_0^{\infty} dE_R \frac{dR}{dE_R} {\rm Poiss}(n|\nu(E_R)), \tag{II.30}$$

where the ${\rm Poiss}(n|\nu(E_R))$ is the Poisson distribution which is given by :

$${\rm Poiss}(k|\lambda) = \frac{\lambda^k e^{-\lambda}}{k!}. \tag{II.31}$$

The Poisson distribution gives the probability of the number of λ event when the number of k events is measured.

(a) Statistical analysis

According to the modified event rate, we can find the number of expected event in a certain energy range or just event rate is enough with respect to a certain experiment. To find validity of the expected quantity about observed quantity in parameter spaces such as $(m_\chi, \sigma_{\rm nucleon})$, the statistical interpretation has to be concerned.

When the event rate is represented in the energy such the DAMA experiment, we can find confidence region using the χ^2–distribution which is written as

$$\chi^2 = \sum_{i=1}^{n} \frac{(S_{m,i}^{\rm obs} - S_{m,i}^{\rm exp})^2}{\sigma_i^2}, \tag{II.32}$$

where the n is the number of data, the $S_{m,i}^{\rm obs}$ is experiment result, the $S_{m,i}^{\rm exp}$ is expected value and the σ_i is the experimental error corresponding to $S_{m,i}^{\rm obs}$. The expected value can be written as $S_{m,i}^{\rm obs}(m_\chi, \sigma_{\rm nucleon}) = \sigma_{\rm nucleon} \times S_{m,i}^{\rm obs}(m_\chi)|_{\sigma_{\rm nucleon}=1}$ to represent in the WIMP mass and nucleon cross section parameter space. According to the χ^2–distribution, the confidence region is presented in $(m_\chi, \sigma_{\rm nucleon})$ parameter space with the number of degrees of freedom.

On the other hand, when experimental results are experiment result is presented as an event in the energy, we can use the maximum gap method (Yellin's method)[73]. This approach calculates the number of expected signal x_i in the gap between any E_i and E_{i+1} corresponding

to closed two events which can be found by

$$x_i = \int_{E_i}^{E_{i+1}} \frac{dR}{dE_R} dE_R. \tag{II.33}$$

The probability in this method is written as

$$P(x,\mu) = \sum_{k=0}^{m} \frac{(kx-\mu)^k e^{-kx}}{k!} \left(1 + \frac{k}{\mu - kx}\right), \tag{II.34}$$

where m is the greatest integer of μ/x, x is the maximum of x_is and μ is the number of total expected signal. When the null signal experiment, it gives same values with Poisson probability distribution. Also, when the experiment result is presented by the number of event with corresponding known background, we can use the Feldman–Cousins method[3].

D. Generalized analysis

In the standard analysis, we assumed the velocity distribution as Maxwellian distribution and WIMP–nucleus interactions as SI coupling and SD coupling. However, we can analyze the direct detection with inelastic dark matter[74, 75], halo–independent method[76] which can neglect the velocity distributions and model–independent WIMP–nucleus cross section from non–relativistic Effective Field Theory

(EFT)[64].

(1) Halo-independent method

A merit of the halo–independent method is that astrophysics uncertainty in direct detection analysis can be neglected without any assumptions. In standard approach, assumptions such as Maxwellian, tidal stream and Debris, the velocity distribution have to be imposed which give uncertainties with respect to real WIMP velocity distribution. However, the halo–independent method suggests another comparison analysis[76] with focusing the $\eta(v_{\rm min})$ because the velocity distribution gives same presentation in each event rate corresponding to experiments.

The halo–independent method[77, 78, 79] estimates the factorized quantity which is defined as

$$\tilde{\eta}(v_{\rm min}) \equiv \frac{\rho_0 \sigma_0}{m_\chi} \eta(v_{\rm min}). \tag{II.35}$$

The total number of expected events, $N_{\rm exp}$, in a certain range $[E_1, E_2]$ can be found by :

$$N_{\rm exp} = \int_{E_1}^{E_2} dE_R \frac{dR}{dE_R} = \int_0^\infty \tilde{\eta}\left[v_{\rm min}(E')\right] \mathcal{R}_{[E_1,E_2]}(E') dE', \tag{II.36}$$

where the $\mathcal{R}_{[E_1,E_2]}(E')$ is response function which is defined as :

$$\mathcal{R}_{[E_1,E_2]}(E') = \frac{N_T}{2\mu^2_{\chi,\text{nucleus}}} F\left[q(E')\right]^2 \int_{E_1}^{E_2} dE_R\, \epsilon(E_R) G(E_R, E'). \tag{II.37}$$

The N_{exp} can be assumed by observed events, therefore average of the factorized quantity $\bar{\tilde{\eta}}$ in the range $[E_1, E_2]$ reads

$$\bar{\tilde{\eta}}_{[E_1,E_2]} = \frac{1}{N_0} \int_0^\infty dE'\, \tilde{\eta}\left[v_{\text{min}}(E')\right] \mathcal{R}_{[E_1,E_2]}(E') = \frac{N_{\text{obs}}}{N_0} \tag{II.38}$$

where N_{obs} is normalized by

$$N_0 = \int_0^\infty dE'\, \mathcal{R}_{[E_1,E_2]}(E')\,. \tag{II.39}$$

The $\bar{\tilde{\eta}}$ is a comparable quantity with experiments in the $v_{\text{min}} - \tilde{\eta}$ plane. In [77, 78, 79, 80], the $\tilde{\eta}$ is assumed with the Heaviside–theta function due to $f(v) \geq 0$ which is represented as $\tilde{\eta}(v_{\text{min}}) = \tilde{\eta}(v'_{\text{min}})\Theta(v'_{\text{min}} - v_{\text{min}})$ for null signal experiments. Among these assumption, it gives the upper bound such that

$$\bar{\tilde{\eta}}_{[E_1,E_2]}(v_0) = N_{\text{obs}} \left[\int_0^{v_0} dE'\, \mathcal{R}_{[E_1,E_2]}(E')\right]^{-1}. \tag{II.40}$$

However, when the other types of experiments which give excess signal or null signal in dR/dE_R, it can be found directly by Eq(II.38) fixing energy interval in the $v_{\text{min}} - \tilde{\eta}$ plane.

In this thesis, however, we fix energy ranges to remove the Heaviside–theta assumption. In this way, we choose the energy ranges corresponding to the DAMA data which is presented from 2keV$_{ee}$ to 4keV$_{ee}$ in bins of 0.5keV$_{ee}$ width. The crucial advantage of this method is that it can be found the compatibility quantitatively.

The halo–independent method suggests the best way to neglect the astrophysical uncertainty. According to the v_{min} is determined by target nucleus, however, it gives complexity when more than two targets are presented in the experiment. For instance, when corresponding velocity ranges of two target nucleuses are overlapped, it should take fraction of contributions of each target nucleus. A way to calculate for multi–target detector is suggested in [80]. In this thesis, the result is separately presented to light mass WIMP due to Sodium and heavy mass due to Iodine. Moreover, we will also introduce a general halo–independent method to estimate conservative upper bound on η for multi–target detectors[81].

(2) Inelastic dark matter

To alleviate the tension between direct detection experiments, the inelastic dark matter(IDM) model is proposed [74]. In this model, according to two mass eigenstates

m_χ and $m_{\chi'}$ of the WIMP, incoming WIMP χ with mass m_χ up–scatters to χ' with mass $m_{\chi'} = m_\chi + \delta$ where δ is mass splitting. On the other hand, exothermic WIMP which the incoming metastable WIMP χ down–scatters to χ' with mass $m_{\chi'} = m_\chi + \delta$ with $\delta < 0$ [75]. The IDM case the kinematic relation Eq(II.10) can be calculated as

$$v_{\rm min} = \frac{1}{\sqrt{2m_{\rm N}E_R}} \left| \frac{m_{\rm N}E_R}{\mu^2_{\chi,\rm nucleus}} + \delta \right| \tag{II.41}$$

The IDM relaxes importance of the threshold because the expected rate is no more decreasing exponentially due to the form factor. According to the form factor, the expected rate is concentrated at $E_R = 0$ while IDM case the $E_R = 0$ when $v_{\rm min} \to \infty$. In particular, the minimum values $v_{\rm min}$ in the cases when $E_R = |\delta|\mu_{\chi,\rm nucleus}/m_{\rm N} \equiv E^*_R$ is given by:

$$v^*_{\rm min} = \begin{cases} \sqrt{\frac{2\delta}{\mu_{\chi,\rm nucleus}}} & ,\delta > 0 \\ 0 & ,\delta < 0. \end{cases} \tag{II.42}$$

Moreover, due to the escape velocity limit, the δ has upper bound such as

$$\delta_{\rm limit} = \frac{\mu_{\chi,\rm nucleus} v^2_{\rm esc}}{2}. \tag{II.43}$$

(3) Non relativistic Effective Field Theory

The SI and SD interactions in the standard analysis are motivated by high energy physics. However, using the model–independent cross section also desirable motivation of direct detection analysis. For instance, in the momentum dependence case[82], the event rate can be factorized as

$$\frac{dR^{\rm MD}}{dE_R} = \left(\frac{q^2}{q^2_{\rm ref}}\right)^n \left(\frac{q^2_{\rm ref} + m^2_\phi}{q^2 + m^2_\phi}\right)^2 \left(\frac{dR}{dE_R}\right), \tag{II.44}$$

where $q^2_{\rm ref}$ is chosen to normalize, m_ϕ is mediator mass and the n is chosen by operators.

On the other hand, in this thesis the generalized cross section using non–relativistic effective field theory (EFT) approach[64, 65] is adopted. In this approach, the general Hamiltonian density is defined as :

$$\mathcal{H} = \sum_{i=1}^{15} \left(c^0_i 1 + c^1_i \tau_3\right) \mathcal{O}_i, \tag{II.45}$$

where $\mathcal{O}_i$ are Hermitian operator when they are constructed out of five three–vectors;

$$1_{\chi N}, \quad i\vec{q}, \quad \vec{v}^{\perp}, \quad \vec{S}_\chi, \quad \vec{S}_N, \tag{II.46}$$

where $1_{\chi N}$ is identity operator, $\vec{q}$ is the transferred momentum, $\vec{v}^{\perp} \equiv \vec{v} + \frac{\vec{q}}{2\mu_{\chi,\text{nucleon}}}$ which satisfies $\vec{v}^{\perp} \cdot \vec{q} = 0$ and $\vec{S_\chi}$ and $\vec{S_N}$ are the WIMP and nucleon operator, respectively. Here, c_i^0 and c_i^1 relate with proton and neutron components such that

$$\begin{aligned} c_i^0 &= \frac{1}{2}\left(c_i^p + c_i^n\right), \\ c_i^1 &= \frac{1}{2}\left(c_i^p - c_i^n\right), \end{aligned} \tag{II.47}$$

and 1 and τ_3 are isospin operators such that :

$$\begin{aligned} 1 &= \text{Identity matrix}, \\ \tau_3 &= \begin{pmatrix} 1 & 0 \\ 0 & -1 \end{pmatrix}. \end{aligned} \tag{II.48}$$

The $\mathcal{O}_i$ are constructed of 15 operator where the 11 operators which associate with spin–0 or spin–1 mediators are:

$$\begin{gathered} \mathcal{O}_1 = 1_\chi 1_N, \quad \mathcal{O}_2 = (\vec{v}^{\perp})^2, \quad \mathcal{O}_3 = i\vec{S}_N \cdot \left(\tfrac{\vec{q}}{m_N} \times \vec{v}^{\perp}\right), \\ \mathcal{O}_4 = \vec{S}_\chi \cdot \vec{S}_N, \quad \mathcal{O}_5 = i\vec{S}_\chi \cdot \left(\tfrac{\vec{q}}{m_N} \times \vec{v}^{\perp}\right), \quad \mathcal{O}_6 = \left(\vec{S}_\chi \cdot \tfrac{\vec{q}}{m_N}\right)\left(\vec{S}_N \cdot \tfrac{\vec{q}}{m_N}\right), \\ \mathcal{O}_7 = \vec{S}_N \cdot \vec{v}^{\perp}, \quad \mathcal{O}_8 = \vec{S}_\chi \cdot \vec{v}^{\perp}, \quad \mathcal{O}_9 = i\vec{S}_\chi \cdot \left(\vec{S}_N \times \tfrac{\vec{q}}{m_N}\right), \\ \mathcal{O}_{10} = i\vec{S}_N \cdot \tfrac{\vec{q}}{m_N}, \quad \mathcal{O}_{11} = i\vec{S}_\chi \cdot \tfrac{\vec{q}}{m_N}, \end{gathered} \tag{II.49}$$

and 4 operators which can not be constructed by spin–0 or spin–1 mediators are :

$$\begin{aligned} \mathcal{O}_{12} &= \vec{S}_\chi \cdot \left(\vec{S}_N \times \vec{v}^{\perp}\right), & \mathcal{O}_{13} &= i\left(\vec{S}_\chi \cdot \vec{v}^{\perp}\right)\left(\vec{S}_N \cdot \frac{\vec{q}}{m_N}\right), \\ \mathcal{O}_{14} &= i\left(\vec{S}_\chi \cdot \frac{\vec{q}}{m_N}\right)\left(\vec{S}_N \cdot \vec{v}^{\perp}\right), & \mathcal{O}_{15} &= -\left(\vec{S}_\chi \cdot \frac{\vec{q}}{m_N}\right)\left[\left(\vec{S}_N \times \vec{v}^{\perp}\right) \cdot \frac{\vec{q}}{m_N}\right]. \end{aligned} \tag{II.50}$$

According to operators $\mathcal{O}_i$, the WIMP–nucleus scattering amplitude can be factorized to particle and nuclear physics term such that :

$$\begin{aligned} &\frac{1}{2j_\chi + 1}\frac{1}{2j_N + 1}\left|\mathcal{M}\right|^2 \\ &\qquad = \frac{4\pi}{2j_N + 1}\sum_{\tau=0}^{1}\sum_{\tau'=0}^{1}\sum_k R_k^{\tau\tau'}\left[c_k^\tau, c_k^{\tau'}, \left(\vec{v_T}^{\perp}\right)^2, \frac{\vec{q}^2}{{m_N}^2}\right] W_k^{\tau\tau'}(q^2), \end{aligned} \tag{II.51}$$

where j_χ and j_T are spin of the WIMP and nucleus, respectively. The $R_k^{\tau\tau'}$ are WIMP response functions and $W_k^{\tau\tau'}$ are nuclear response function. The index k categorize corresponding WIMP–nucleus interaction type such as SI or SD to effective nuclear operators, while the [65] represents 8 operators using the Wigner-Eckart theorem such as $k = M,\ \Phi'',\ \tilde{\Phi}',\ \Sigma'',\ \Sigma',\ \Delta,\ \Phi''M,\ \Delta\Sigma'$ within the assumptions that nuclear ground state is an eigenstate of P and CP. The categorization recast the WIMP

response function $R_k^{\tau\tau'}$ as :

$$
\begin{aligned}
R_M^{\tau\tau'}\left(v_T^{\perp 2},\tfrac{q^2}{m_N^2}\right) &= c_1^\tau c_1^{\tau'} + \tfrac{j_\chi(j_\chi+1)}{3}\left[\tfrac{q^2}{m_N^2}v_T^{\perp 2}c_5^\tau c_5^{\tau'} + v_T^{\perp 2}c_8^\tau c_8^{\tau'} + \tfrac{q^2}{m_N^2}c_{11}^\tau c_{11}^{\tau'}\right] \\
R_{\Phi''}^{\tau\tau'}\left(v_T^{\perp 2},\tfrac{q^2}{m_N^2}\right) &= \left[\tfrac{q^2}{4m_N^2}c_3^\tau c_3^{\tau'} + \tfrac{j_\chi(j_\chi+1)}{12}\left(c_{12}^\tau - \tfrac{q^2}{m_N^2}c_{15}^\tau\right)\left(c_{12}^{\tau'} - \tfrac{q^2}{m_N^2}c_{15}^{\tau'}\right)\right]\tfrac{q^2}{m_N^2} \\
R_{\Phi''M}^{\tau\tau'}\left(v_T^{\perp 2},\tfrac{q^2}{m_N^2}\right) &= \left[c_3^\tau c_1^{\tau'} + \tfrac{j_\chi(j_\chi+1)}{3}\left(c_{12}^\tau - \tfrac{q^2}{m_N^2}c_{15}^\tau\right)c_{11}^{\tau'}\right]\tfrac{q^2}{m_N^2} \\
R_{\tilde{\Phi}'}^{\tau\tau'}\left(v_T^{\perp 2},\tfrac{q^2}{m_N^2}\right) &= \left[\tfrac{j_\chi(j_\chi+1)}{12}\left(c_{12}^\tau c_{12}^{\tau'} + \tfrac{q^2}{m_N^2}c_{13}^\tau c_{13}^{\tau'}\right)\right]\tfrac{q^2}{m_N^2} \\
R_{\Sigma''}^{\tau\tau'}\left(v_T^{\perp 2},\tfrac{q^2}{m_N^2}\right) &= \tfrac{q^2}{4m_N^2}c_{10}^\tau c_{10}^{\tau'} + \tfrac{j_\chi(j_\chi+1)}{12}\left[c_4^\tau c_4^{\tau'} + \tfrac{q^2}{m_N^2}(c_4^\tau c_6^{\tau'} + c_6^\tau c_4^{\tau'}) + \right. \\
&\qquad \left. \tfrac{q^4}{m_N^4}c_6^\tau c_6^{\tau'} + v_T^{\perp 2}c_{12}^\tau c_{12}^{\tau'} + \tfrac{q^2}{m_N^2}v_T^{\perp 2}c_{13}^\tau c_{13}^{\tau'}\right] \\
R_{\Sigma'}^{\tau\tau'}\left(v_T^{\perp 2},\tfrac{q^2}{m_N^2}\right) &= \tfrac{1}{8}\left[\tfrac{q^2}{m_N^2}v_T^{\perp 2}c_3^\tau c_3^{\tau'} + v_T^{\perp 2}c_7^\tau c_7^{\tau'}\right] + \tfrac{j_\chi(j_\chi+1)}{12}\left[c_4^\tau c_4^{\tau'}\right. \\
&\qquad + \tfrac{q^2}{m_N^2}c_9^\tau c_9^{\tau'} + \tfrac{v_T^{\perp 2}}{2}\left(c_{12}^\tau - \tfrac{q^2}{m_N^2}c_{15}^\tau\right)\left(c_{12}^{\tau'} - \tfrac{q^2}{m_N^2}c_{15}^{\tau\prime}\right) \\
&\qquad \left. + \tfrac{q^2}{2m_N^2}v_T^{\perp 2}c_{14}^\tau c_{14}^{\tau'}\right] \\
R_{\Delta}^{\tau\tau'}\left(v_T^{\perp 2},\tfrac{q^2}{m_N^2}\right) &= \tfrac{j_\chi(j_\chi+1)}{3}\left(\tfrac{q^2}{m_N^2}c_5^\tau c_5^{\tau'} + c_8^\tau c_8^{\tau'}\right)\tfrac{q^2}{m_N^2} \\
R_{\Delta\Sigma'}^{\tau\tau'}\left(v_T^{\perp 2},\tfrac{q^2}{m_N^2}\right) &= \tfrac{j_\chi(j_\chi+1)}{3}\left(c_5^\tau c_4^{\tau'} - c_8^\tau c_9^{\tau'}\right)\tfrac{q^2}{m_N^2}.
\end{aligned}
\tag{II.52}
$$

The WIMP response functions in Eq(II.52) presents dependences q^2, q^4 and $(\vec{v}^\perp)^2$. In particular, according to the $(\vec{v}^\perp)^2 = v^2 - v_{\min}^2$, the $R_k^{\tau\tau'}$ can decompose to

$$
R_k^{\tau\tau'} = R_{0k}^{\tau\tau'} + R_{1k}^{\tau\tau'}(\vec{v}^\perp)^2 = R_{0k}^{\tau\tau'} + R_{1k}^{\tau\tau'}(\vec{v}^2 - v_{\min}^2). \tag{II.53}
$$

The nuclear response function $W_k^{\tau\tau'}$ is calculated for each nucleus using nuclear shell model, numerically (provided in [64, 65, 66], Especially, [65] presents *Mathematica*

script).

CHAPTER III

RESULTS

In this chapter, it will show the new approach which is adopted the generalized analysis. The results are categorized as IDM with SI interaction[83], elastic spin–dependent dark matter[81] and IDM with model–independent cross section based on the halo–independent method. In particular, the halo–independent method is adopt with special mapping in velocity range which corresponds to energy in each experiments. It implies that, in the result, the basic estimation Eq(II.38) recast as

$$\bar{\tilde{\eta}}_{[v_{\min,1},v_{\min,2}]} = \frac{\int_0^{v_{\rm esc}} dv_{\rm min}\bar{\eta}(v_{\rm min})\mathcal{R}_{[E'_1,E'_2]}(v_{\rm min})}{\int_0^{v_{\rm esc}} \mathcal{R}_{[E'_1,E'_2]}(v_{\rm min})} = \frac{N_{\rm obs}}{\int_0^{v_{\rm esc}} \mathcal{R}_{[E'_1,E'_2]}(v_{\rm min})}, \quad \text{(III.1)}$$

where $[v_{\min,1}, v_{\min,2}]$ corresponds to energy interval $[E_{ee,1}, E_{ee,2}]$ where $E_{ee,1} = E'_1 - \sigma_{\rm res}$ and $E_{ee,2} = E'_2 + \sigma_{\rm res}$ (E_{ee} represents electron equivalent energy due to quenching effect). Moreover, the notation $\bar{\tilde{\eta}}_0$ and $\bar{\tilde{\eta}}_1$ indicates unmodulation and modulation

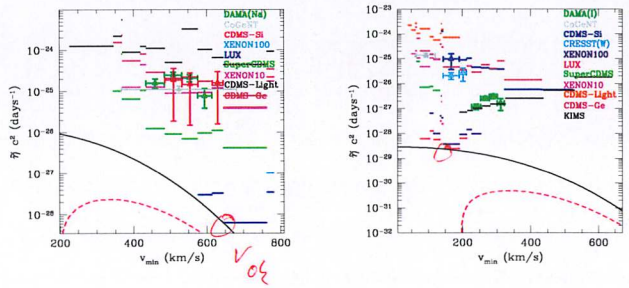

Figure III.1: Measurement and bounds for $f_p/f_n = 1$. The horizontal line presents 90% C.L. upper bound which are given by null signal. The error bar in x–y axis presents 90%C.L of excesses. The green data shows DAMA which presents modulation $\bar{\tilde{\eta}}_1$. The black continuous solid line shows the Maxwellian velocity distribution which is normalized by most constraining upper bound and the red dashed line shows modulated distribution in the same normalization **Left** : $m_\chi = 8$GeV (Only sodium is valid in DAMA) **Right** : $m_\chi = 100$GeV(Only iodine is valid in DAMA)

result, respectively.

A. IDM with SI interaction using the halo-independent method

Following result is applied the IDM, SI and halo–independent method[83]. This result takes into account the DAMA, CoGeNT,CDMS–Si, Xenon100, LUX, Super CDMS,

Xenon10, CDMS–light and CDMS–Ge experiments. First, we remap experimental data in the same $v_{\rm min}$ from the DAMA experimental data which has the highest accumulated statistics. Outside of DAMA data, the mapping follows each experiments region of interest(ROE). In the elastic case and SI interaction, the result is shown in the Fig.(III.1). On the other hand for inelastic scattering the relation between energy and $v_{\rm min}$ changes as a function of δ due to Eq(II.41), so if the halo–independent methods is adapted the data need to be rebinned. In some of case of the IDM, taking the given DAMA data without modifications may caused problem, when the $E_{ee}(E_R^*) \in [E_i, E_{i+1}]$, where the $[E_i, E_{i+1}]$ is i–th energy range of the DAMA. In this case, integral of Eq(III.1) is disconnected due to overlapping in the $v_{\rm min}$ space. Therefore, we modify the $v_{\rm min}$ range from the $v_{\rm min}^*$ corresponding to E_R^* with statistically allowed energy range to avoid overlapping. Furthermore, we define rebinned DAMA data with respect to a changed $v_{\rm min}$ range such as

$$S_m^{\rm rebinned}(E_{\rm min}, E_{\rm max}) = \frac{1}{\Delta E}\sum_i \Delta_{{\rm O.L.},i} E_i S_{m,i}, \tag{III.2}$$

where $E_{\rm min}$ and $E_{\rm max}$ are the minimum and maximum of new energy range, respectively, $\Delta E = E_{\rm max} - E_{\rm min}$, $\Delta_{{\rm O.L.},i}E_i$ is degree of overlapped energy range between new and i–th energy range of original and $S_{m,i}$ is original data.

On the other hand, to interpret compatibility of results, we can make the smallest

possible assumptions such that :

$$\begin{aligned} &\tilde{\eta}_0(v_{\rm min,2}) \le \tilde{\eta}_0(v_{\rm min,1}) \quad \text{if } v_{\rm min,2} > v_{\rm min,1}, \\ &\tilde{\eta}_0(v_{\rm min} \ge v_{\rm esc}) = 0, \\ &\tilde{\eta}_1(v_{\rm min}) \le \tilde{\eta}_0(v_{\rm min}). \end{aligned} \tag{III.3}$$

The first is due to the fact that η_0 is a decreasing function of $v_{\rm min}$ Eq(II.23), the second is due to the fact that the velocity is cut at $v_{\rm esc}$ due to that the WIMP bounds on gravitational potential and the third is due to the fact that η_1 is the modulated part of η_0. In this result we assume that the $v_{\rm esc} = 782$km/s in the laboratory rest frame which is the combination of escape velocity in the Galaxy rest frame, $v_{\rm esc}^{\rm Galaxy} = 550$km/s, and the Solar system velocity $v_0 = 232$km/s.

In the IDM case, the $v_{\rm min}$ can be have same energy ranges corresponding to different energy ranges. The procedure of selection of energy ranges is that when we choose an energy range E_SIG then map to energy range which give same $v_{\rm min}$ range, M_E_SIG as shown Fig(III.2). There are two possible chosen while the red range in Fig(III.2) is not valid due to the fact that the M_E_SIG is not in the ROE. According to the ranges, it can be considered a self–consistency checking for DAMA which the data is given by excess. If one energy range has excess but the other corresponding energy range is not, it should exclude by self, roughly. Using statistical approach[84],

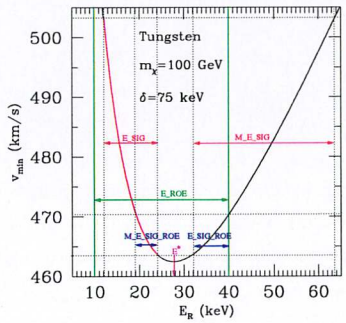

Figure III.2: Relation between $v_{\rm min}$ and recoil energy with Tungsten in CRESST, $m_\chi = 100$GeV and $\delta = 75$keV. ROE is green solid vertical lines.

we can find that :

$$\Delta_{\rm ST} \equiv \frac{\bar{\tilde{\eta}}_{1,1} - \bar{\tilde{\eta}}_{1,2}}{\sqrt{\sigma_1^2 + \sigma_2^2}} \leq 1.64 \tag{III.4}$$

at the 95% C.L due to large statistic data of DAMA, where $\bar{\tilde{\eta}}_{1,1}$ and $\bar{\tilde{\eta}}_{1,2}$ are modulated value for a energy range and its mirror range, respectively, and σ_1 and σ_2 are corresponding deviation from DAMA data. On the other hand, other experiments excesses which is presented by absolute rates and the statistic is lower than DAMA are assumed Possonian fluctuation. To check the self–consistency, the Przyborowski and Wilenski[85] is adopted to check if the two count rates N_1 and N_2 belong to the same Poisson distribution. The p–value for the hypothesis $\lambda_1/\lambda_2 \leq c$ with λ_1 and λ_2

the corresponding averaged values of the two Possonians with :

$$\frac{\lambda_1}{\lambda_2} \leq c = \frac{\int_0^\infty dE_{ee} \mathcal{R}_{\rm E\_SIG}(E_{ee})}{\int_0^\infty dE_{ee} \mathcal{R}_{\rm M\_E\_SIG}(E_{ee})}, \tag{III.5}$$

is given by :

$$p = \sum_{n=N_1}^{N_1+N_2} \left(\begin{array}{c} N_1+N_2 \\ n \end{array} \right) f(c)^n \Big(1 - f(c)\Big)^{N_1+N_2-n}, \tag{III.6}$$

where $f(c) = c/(1+c)$. The $p \geq 0.05$ 95% C.L..

In this result, the IDM parameter space is analyzed using the parameter ranges:

$$1 \text{ GeV} \leq m_{DM} \leq 1 \text{ TeV}, -300 \text{ keV} \leq \delta \leq 300 \text{ keV}. \tag{III.7}$$

and considered targets are Sodium (DAMA), Iodine (DAMA and KIMS), Germanium (CDMS–Ge, SuperCDMS, CoGeNT and CDMS–light), Silicon (CDMS–Si), Tungsten (CRESST) and Xenon (LUX, Xenon100 and Xenon10). In particular, the DAMA is concerned the second assumption in Eq(III.3) because the WIMP candidate excess has to be taken only the gravitational bounding ones.

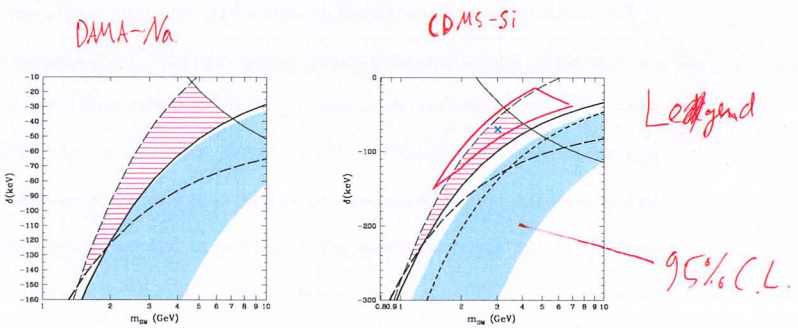

Figure III.3: The horizontal solid red hatched areas show kinematically possible ranges for excesses, DAMA–Na and CDMS–Si in the left and right, respectively. Both figures inside the dashed lines (thin and thick) are V_DAMA_NA and V_DAMA_CDMS ∈ V_GAL (The thin and thick are corresponding to $v_{\rm min}\left(E_{\rm min}^{\rm DAMA,Na}\right) = v_{\rm esc}$ and $v_{\rm min}\left(E_{\rm max}^{\rm DAMA,Na}\right) = v_{\rm esc}$, respectively) while the solid lines are the range comparing between the DAMA and LUX (The thin and thick are corresponding to $v_{\rm min}\left(E_{\rm min}^{\rm LUX}\right) = v_{\rm min}\left(E_{\rm max}^{\rm DAMA,Na}\right)$ and $v_{\rm min}\left(E_{\rm min}^{\rm LUX}\right) = v_{\rm min}\left(E_{\rm min}^{\rm DAMA,Na}\right)$, respectively). The blue shaded regions in left and right represent allowed region at 95% C.L. due to self consistency checking for sodium and silicon, respectively. The red closed solid line in right figure is the mapping the possible region of sodium in the DAMA corresponding to the left. The cross in overlapped possible region is benchmark in Fig(III.4)

(1) Sodium scattering in DAMA and the CDMS-Si excess

To analyze the kinematically possible range in m_χ–δ parameter space, we indicate the $v_{\rm min}$ ranges with V_GAL $\equiv [0, v_{\rm esc}]$, V_DAMA_NA$\equiv [v_{\rm min}^{\rm DAMA,Na}, v_{\rm max}^{\rm DAMA,Na}]$ the $v_{\rm min}$ range for the DAMA signal assuming scattering on Sodium, and with V_DAMA_I$\equiv [v_{\rm min}^{\rm DAMA,I}, v_{\rm max}^{\rm DAMA,I}]$ the corresponding one for scattering on Iodine. V_LUX $\equiv [v_{\rm min}^{\rm LUX}, v_{\rm max}^{\rm LUX}]$ represents the range to which LUX is sensitive, while the V_XENON100$\equiv [v_{\rm min}^{\rm XENON100}, v_{\rm max}^{\rm XENON100}]$ is the same for XENON100. This result is shown in Fig(III.3) for sodium in DAMA (left) and silicon in CDMS–Si (right). In this result, the region is taken gravitational bounding, which is V_DAMA_NA⊂V_GAL, and evading the overlapping with LUX because it gives most upper bound part in the SI WIMP while, according to the weakness or complication of the halo–independent method to multi–target, the result of sodium and iodine in the DAMA separating out which the relation is V_DAMA_NA∩V_DAMA_I=0 and V_DAMA_I∩V_GAL=0. To evade, we can assume that V_LUX∩V_DAMA_NA=0 and V_LUX>V_DAMA_NA. In addition, when excess is constrained by upper bounds, the way to evasion is to shift the upper bound experiments' $v_{\rm min}$ by δ due to the fact that the δ relates only kinematics. However, the V_SUPERCDMS$\equiv [v_{\rm min}^{\rm SuperCDMS}, v_{\rm max}^{\rm SuperCDMS}]$ can not be reconciled with V_DAMA_NA. Therefore, we adopt Isospin violation mechanism[86, 87, 88] which effective couplings in the SI cross section, Eq(II.12), for the proton and neutron can

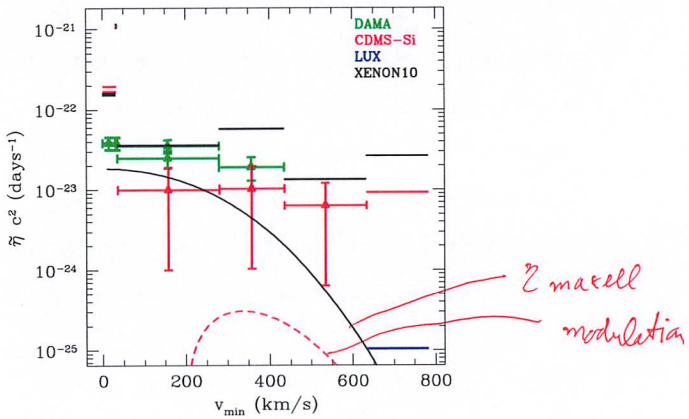

Figure III.4: Result of the function $\tilde{\eta}_0$ and $\tilde{\eta}_1$ of excesses and bounds, which is represented with the crossed and flat solid lines, respectively, for the benchmark point $m_\chi = 3\text{GeV}$, $\delta = -70\text{keV}$, $f_n/f_p = -0.79$, in Fig(III.3). The continuous solid line(black) is $\eta_{\text{maxwellian}}$ with normalization and dashed(red) line is its modulation.

be suppressed by specific choice of f_n/f_p. In particular, the SuperCDMS bound would no longer present using $f_n/f_p \simeq -0.79$. Also, we repeat the same analysis for V_CDMS-Si$\equiv$ $[v_{\text{min}}^{\text{CDMS-Si}}, v_{\text{max}}^{\text{CDMS-Si}}]$ to LUX, Xenon100 and SuperCDMS. In this case also the Isospin violating mechanism is adopted with same value of $f_n/f_p \simeq -0.79$, hence the V_SUPERCDMS can not be reconciled with V_CDMS_Si. As Fig(III.4) which shows in $v_{\text{min}} - \tilde{\eta}$ space for the benchmark point $m_\chi = 3\text{GeV}$, $\delta = -70\text{keV}$, $f_n/f_p = -0.79$ in Fig(III.3), the upper bounds from LUX and Xenon10 are compatible with DAMA and CDMS–Si excesses $\tilde{\eta}$. However, due to the third assumption in Eq(III.3), DAMA and CDMS–Si has tension even velocity distribution is not assumed. Moreover, due to that the continuous solid line(black) is $\eta_{\text{maxwellian}}$ normalized to the most constraining upper bound, Maxwellian distribution is exclude by CDMS–Si excess in a bit and also the modulated η_1s by the DAMA and Maxwellian distribution with same normalization which is dashed line(red) do not compatible in the whole range.

(2) Iodine scattering in DAMA and CRESST

In this section, we will analyze iodine in DAMA and tungsten in CRESST. In the elastic scattering result as shown in Fig(III.1), iodine result in DAMA is constrained by KIMS. However, it can not be solved discrepancy as for sodium in DAMA with LUX or SuperCDMS since the target of KIMS is same with DAMA. On the other

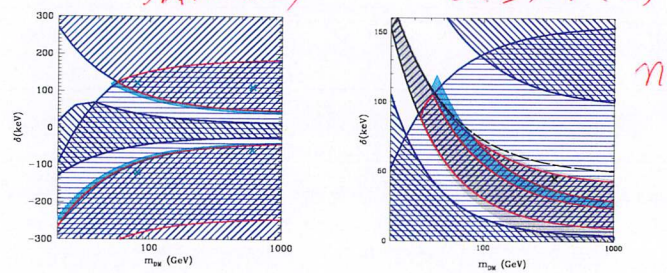

Figure III.5: Same as Fig(III.3) for iodine in DAMA(left) and tungsten in CRESST(right).

hand, the tension with other experiments can be alleviated by the isospin violating mechanism and kinematic relation which the bounds can be shifted to left for allowing the second condition in Eq(III.3). Fig(III.5) shows the possible regions for DAMA(left) and CRESST(right) in $m_\chi - \delta$ parameter space. In the iodine in DAMA, the whole range in Fig(III.5) is V_DAMA_NA∩V_GAL=0 to evade overlapping between sodium and iodine while the horizontal solid lines corresponds to V_DAMA_I ⊂ V_GAL. Moreover, shaded areas(light–blue) are forbidden regions by the self–consistency checking. The $+45°$ oblique solid lines present V_LUX>V_DAMA_I and the $-45°$ oblique solid lines present V_SUPERCDMS<V_DAMA_I. Moreover, the boundaries of $+45°$ oblique lines are determined by a combination of two conditions: $v_{\rm min}(E^{\rm LUX}_{\rm max}) = v_{\rm min}(E^{\rm DAMA,I}_{\rm min})$ and $v_{\rm min}(E^{\rm LUX}_{\rm max}) = v_{\rm min}(E^{\rm DAMA,I}_{\rm max})$ and also $-45°$ oblique lines are same feature between DAMA and SuperCDMS. In particular, the overlapping region between horizontal and $-45°$ line are compatible when we compare only SuperCDMS and DAMA due to the fact that the SuperCDMS upper bound is larger than DAMA as shown Fig(III.1), while the LUX upper bound exclude the DAMA when $+45°$ and horizontal lines are not overlapped. Therefore, the possible region is presented in the closed solid line(red). Moreover, when Xenon 100 is adopted which the energy range is larger than LUX, the possible range is going smaller than Fig(III.5) and ,as we will see, the Xenon 100 could not be compatible with DAMA. The left panel in Fig(III.5) is analyzed with tungsten in CRESST. The horizontal lines are V_CRESST_W⊂V_GAL, where V_CRESST_W≡ $[v^{\rm CRESST,W}_{\rm min}, v^{\rm CRESST,W}_{\rm max}]$. Although the other targets calcium and oxygen are not always beyond $v_{\rm esc}$, the most dominant signal is tungsten which is the heaviest target due to Eq(II.12). Moreover, $+45°$ oblique line presents V_LUX>V_CRESST_W and $-45°$ oblique line presents V_SUPERCDMS<V_CRESST_W. The shaded area(blue) is forbidden by self–consistency checking. The boundaries conditions are same with iodine when tungsten substitutes for iodine. On the other hand, it should be checked with KIMS experiment according. According to Fig(III.1), it could be compatible when the V_KIMS>V_CRESST_W, where V_KIMS≡ $[v^{\rm KIMS}_{\rm min}, v^{\rm KIMS}_{\rm max}]$ which is shown as shaded area (gray) in Fig(III.5), while a tension from KIMS can be neglected. Fig(III.6) and Fig(III.7) are result

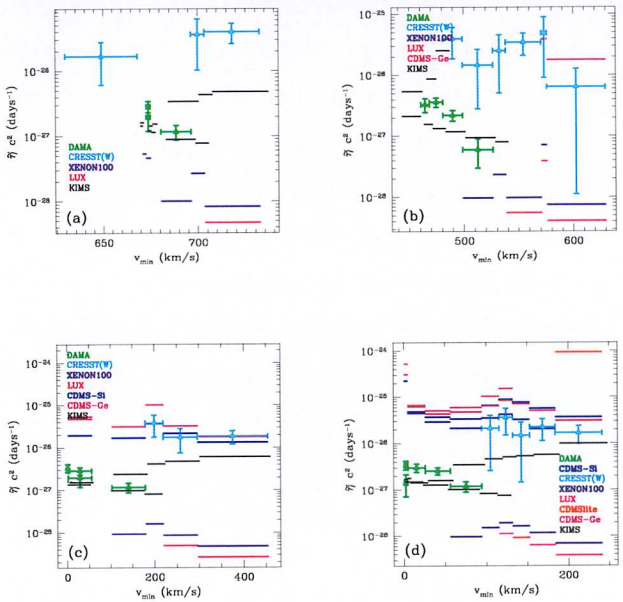

Figure III.6: Result of the function $\tilde{\eta}_0$ and $\tilde{\eta}_1$ of excesses and bounds, which is represented with the crossed and flat solid lines, respectively, for the benchmark points in the left panel of Fig(III.5) for $f_n/f_p = 1$. **(a)** m_χ =80 GeV, δ=120 keV; **(b)** m_χ =600 GeV, δ=110 keV; **(c)** m_χ =80 GeV, δ=-120 keV; **(d)** m_χ =600 GeV, δ=-60 keV.

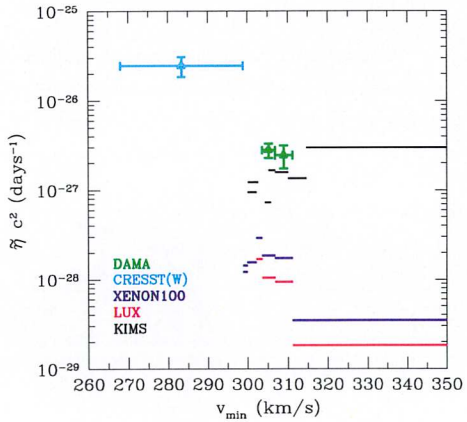

Figure III.7: Result of the function $\tilde{\eta}_0$ and $\tilde{\eta}_1$ of excesses and bounds, which is represented with the crossed and flat solid lines, respectively, for the benchmark point in the right panel of Fig(III.5) for $f_n/f_p = 1$, $m_\chi = 350$ GeV, δ=45 keV

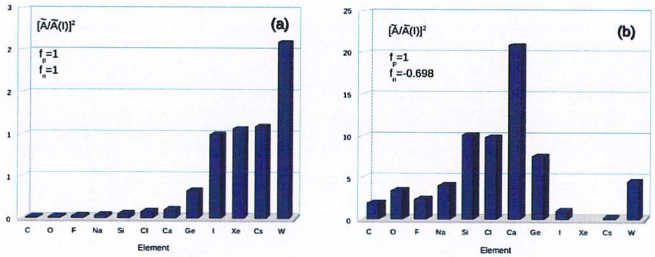

Figure III.8: The values of $\tilde{A}$ with normalized to iodine $\tilde{A}$. **(a)** f_n/f_p=1. **(b)** Isospin violating case f_n/f_p=-0.698, corresponding to the maximal suppression of the WIMP coupling to Xenon targets.

in $v_{\min} - \tilde{\eta}$ plane corresponding to benchmark point in Fig(III.5). Iodine DAMA result shows that with the exception of KIMS and Xenon100, the other constraints are compatible with DAMA. Also, Fig(III.7) result shows that the CRESST can be compatible with constraints, while the total compatibility can not be. On the other hand, we can also adopt the isospin violation mechanism. As the light mass of WIMP, the fraction is chosen as $f_n/f_p = -0.79$ to suppress SuperCDMS. In iodine case, however, the tension from SuperCDMS is no longer strong, while a crucial tension is due to Xenon 100. Therefore, we take the $f_p = 1$ and $f_n = -0.698$ as shown Fig(III.8), where $\tilde{A} \equiv Z + (A - Z)f_n/f_p$. According to the Fig(III.8), the possible range checking should take the calcium and oxygen which are enhanced by particular choice of f_n/f_p. Possible region in $m_\chi - \delta$ parameter space is shown in the left in

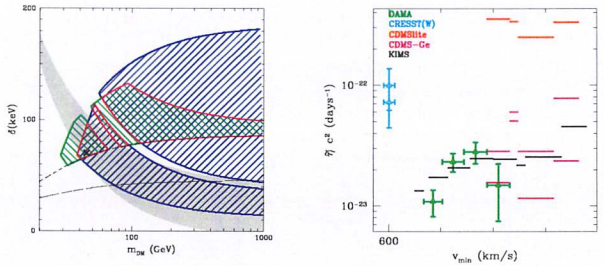

Figure III.9: **Left)** Possible region checking in $m_\chi - \delta$ parameter space to compatible with SuperCDMS and CRESST. **Right)** Result of the function $\tilde{\eta}_0$ and $\tilde{\eta}_1$ of excesses and bounds, which is represented with the crossed and flat solid lines, respectively, for the benchmark points in the left panel for $f_n/f_p = -0.689$.

Fig(III.9). $+45°$ oblique line(blue) is allowed region for iodine in DAMA and $-45°$ oblique line(green) is possible region for tungsten in CRESST as shown Fig(III.5). Due to the enhancement of calcium and oxygen in CRESST when $f_n/f_p = -0.689$, parameter space scanning in the case of that those targets V_CRESST_Ca∩V_GAL=0 and V_CRESST_O∩V_GAL=0 gives possible ranges which are above the short–dashed line and long–dashed line, respectively. As the result in $v_{\rm min} - \tilde{\eta}$ shown in the right panel in Fig(III.9), DAMA $\tilde{\eta}_1$ is marginally accessed by CDMS–Ge, while the upper bound from KIMS iodine still excludes the DAMA. On the other hand, we calculate $\bar{\tilde{\eta}}$ of the KIMS experiment using CsI–crystal as

$$\bar{\tilde{\eta}} = \frac{\int_0^\infty dv_{\rm min}\tilde{\eta}(v_{\rm min})\left[\mathcal{R}^{\rm Iodine}_{[E'_1,E'_2]}(v_{\rm min}) + \mathcal{R}^{\rm Cesium}_{[E'_1,E'_2]}(v_{\rm min})\right]}{\int_0^\infty dv_{\rm min}\left[\mathcal{R}^{\rm Iodine}_{[E'_1,E'_2]}(v_{\rm min}) + \mathcal{R}^{\rm Cesium}_{[E'_1,E'_2]}(v_{\rm min})\right]}. \tag{III.8}$$

Since the cesium ($A = 133$) and iodine ($A = 127$) atomic number are closed, the fraction between cesium and iodine is same.

nearly the

(3) Sodium scattering at heavy mass

In heavy mass of WIMP scenario, KIMS and DAMA are incompatible if both dominated by WIMP–Iodine scatterings. However, if DAMA is dominated by scattering off sodium, they can be recoincided. In this scenario, the heavy WIMP mass and different quenching factor which is given by $Q_{\rm Na} = 0.024 \times \sqrt{E_R}$ with fitting of shown Fig(9) in

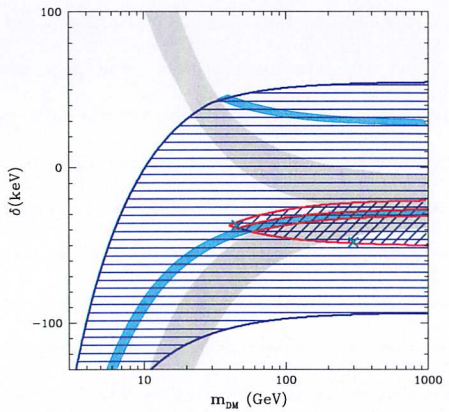

Figure III.10: Possible region for sodium in wider $m_\chi - \delta$ range to find region around the heavy mass

[89] are adopted. In Fig(III.10) closed line (red) is possible region in combinations of following conditions, horizontal line present V_DAMA_NA⊂V_GAL, $= 45°$ oblique line V_SUPERCDMS>V_DAMA_NA, the shaded region (blue) presents forbidden region by self–consistency checking, and the gray presents V_DAMA_NA∩V_DAMA_I$\neq 0$. On the other hand, V_LUX<V_DAMA_NA in the parameter ranges Eq(III.7). Therefore, fraction of coupling constant is taken as $f_n/f_p = -0.69$. The result shown in Fig(III.11) is

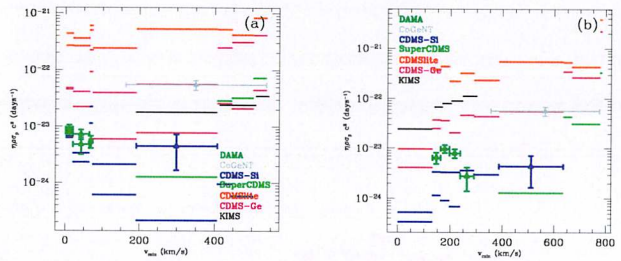

Figure III.11: Result of the function $\tilde{\eta}_0$ and $\tilde{\eta}_1$ of excesses and bounds, which is represented with the crossed and flat solid lines, respectively, for the benchmark points in the left panel for $f_n/f_p = -0.689$.**(a)** m_χ =45 GeV, δ=-37 keV; **(b)** m_χ =300 GeV, δ=-48 keV.

that incompatibility between DAMA and KIMS ,which we saw in Fig(III.6), Fig(III.7) and Fig(III.9), DAMA and DAMA and SuperCDMS which we saw in Fig(III.1) is relaxed. However, DAMA is excluded by the CDMS–Si (a) or both the CDMS–Si and the CDMS–Ge(b) in Fig(III.11)

(4) Conclusion

In the Inelastic Dark Matter scenario, the halo–model factorization approach used to compare results from Dark Matter direct detection experiments is more complicated that in the elastic case, because in presence of a mass splitting $\delta \neq 0$ the mapping

between the nuclear recoil energy E_R and the minimal velocity $v_{\rm min}$ that the incoming WIMP needs to have to deposit E_R becomes more involved than in the elastic case. For this reason a systematic analysis of IDM where all available data are included making use of the factorization property of the halo–model dependence was still missing so far. In the present thesis we have attempted to address this issue, introducing some strategies to determine regions in the IDM parameter space where the tension existing among different experimental results can be (at least partially) alleviated.

To this aim we have first introduced some internal consistency checks involving the data of one single experiment, which exploit the fact that, when the same $v_{\rm min}$ range is mapped in two different energy intervals, the expected correlation can be compared with the data. Moreover, we have argued that, if a minimal set of assumptions is adopted for the WIMP velocity distribution, the tension between the putative signal from an experimental excess and the constraint from a null result can be reduced or eliminated provided that the two results can be mapped into non–overlapping ranges of $v_{\rm min}$ and if the $v_{\rm min}$ range of the constraint is at higher values compared to that of the excess. We stress that this latter argument involves exclusively kinematics, and is valid no matter what the dynamics of the process is.

We have then shown that, in the elastic case, the constraints from XENON100, LUX and SuperCDMS are the most binding, and argued that this hierarchy among

limits is preserved in the IDM case. Then, adopting the two criteria summarized above, we have systematically explored the IDM parameter space to find regions where the XENON100, LUX and the SuperCDMS constraints are relaxed, and picked within those regions some representative benchmark points where we have discussed in more detail the experimental situation including all the other bounds.

Following the strategy outlined above, we have then singled out five scenarios:

i) 2 GeV$\lesssim m_\chi \lesssim$ 4 GeV, -130 keV$\lesssim \delta \lesssim$-45 keV (see Fig(III.3): in this approximate domain both an explanation of the DAMA modulation effect through WIMP–Na scattering and the excess of three WIMP–candidate events observed by CDMS–Si can be brought in agreement with other bounds if some dynamical mechanism such as isospin violation can be advocated to suppress WIMP interaction with germanium. However, the DAMA and CDMS–Si results turn out to be in mutual tension.

ii) $m_\chi \gtrsim$ 60 GeV, 50 keV$\lesssim \delta \lesssim$ 180 keV; a wide band with $\delta \lesssim$ -40 keV (see Fig(III.5)): in this approximate domain the tension between an explanation of the DAMA modulation effect in terms of WIMP–Iodine scattering can be alleviated by reducing it to that with the minimal number of other experiments: KIMS (which uses the same target nucleus) and XENON100 (which turns out to be more constraining than LUX thanks to the higher value of the upper bound

of its analyzed energy region in keVnr). Notice that in the usual case when an Isothermal Sphere model for the velocity distribution is assumed, besides KIMS and XENON100 the DAMA region at large m_χ appears to be well inside the domain excluded also by LUX and/or SuperCDMS (depending on the δ parameter). This may be interpreted as to strengthen the robustness of the exclusion, in spite of the many uncertainties existing in each experiment when taken separately. In our analysis we have shown that sometimes this argument can be misleading, and the number of experiments necessarily in tension with DAMA at large WIMP masses can be lower than generally assumed.

iii) $m_\chi \gtrsim$ 30 GeV, 10 keV$\lesssim \delta \lesssim$ 100 keV (see Fig(III.5)) : in this approximate domain the excess measured by CRESST[67] can be made compatible with all other constraints.

iv) $m_\chi \gtrsim$ 350 GeV, 50 keV$\lesssim \delta \lesssim$ 130 keV (see Fig(III.9)). Mutual compatibility can be achieved between DAMA and CRESST in compliance with other constraints with the exception of KIMS. The size of the corresponding region in the m_χ–δ parameter space varies depending on the f_n/f_p parameter.

v) If a measurement of the Sodium quenching factor substantially smaller compared to other measurements is adopted[89] and assuming a suppression mechanism for the WIMP–Xenon coupling, it is possible to single out a region of

the parameter space with $m_\chi \gtrsim 40$ GeV, -50 keV$\lesssim \delta \lesssim$ -20 keV where WIMP–Sodium scattering dominates in DAMA (see Fig(III.10)). In this regime the SuperCDMS bound is evaded and also KIMS is not constraining. However, now DAMA appears in tension with CDMS–Si and CDMS–Ge.

All the compatibility regions listed above cannot be achieved if a standard Isothermal Sphere is adopted for the WIMP velocity distribution.

B. SD interaction using non-relativistic EFT

In this section, as seen above, the halo–independent method is applied and also, the generalized spin–dependent interaction using non–relativistic EFT[64, 65] while, IDM scenario is no longer imposed[81]. In this analysis, we take DAMA, LUX, SuperCDMS, Xenon10, CDMSlite, CDMS–Ge, SIMPLE, COUPP, PICASSO and PICO–2L. On the other hand, in the SD interaction case the isotopes of atom are important because, this interaction is sensitive to total spin of proton and neutron which are dominantly given by number of proton and neutron.

The Table(III.1) gives nuclear response functions corresponding to each couplings in terms of velocity–independent($\mathcal{R}_0$) and dependent($\mathcal{R}_1$) as written as Eq(II.53). According to [64, 65], the SD interaction is sum of the Σ' and Σ'', which are components of the nucleon spin along the perpendicular and parallel direction of the

coupling	$R_{0k}^{\tau\tau'}$	$R_{1k}^{\tau\tau'}$	coupling	$R_{0k}^{\tau\tau'}$	$R_{1k}^{\tau\tau'}$
1	$M(q^0)$	-	3	$\Phi''(q^4)$	$\Sigma'(q^2)$
4	$\Sigma''(q^0)$,$\Sigma'(q^0)$	-	5	$\Delta(q^4)$	$M(q^2)$
6	$\Sigma''(q^4)$	-	7	-	$\Sigma'(q^0)$
8	$\Delta(q^2)$	$M(q^0)$	9	$\Sigma'(q^2)$	-
10	$\Sigma''(q^2)$	-	11	$M(q^2)$	-
12	$\Phi''(q^2)$,$\tilde{\Phi}'(q^2)$	$\Sigma''(q^0)$,$\Sigma'(q^0)$	13	$\tilde{\Phi}'(q^4)$	$\Sigma''(q^2)$
14	-	$\Sigma'(q^2)$	15	$\Phi''(q^6)$	$\Sigma'(q^4)$

Table III.1: Nuclear response functions corresponding to each coupling, for the velocity–independent and the velocity–dependent components parts of the WIMP response function. In parenthesis the power of q in the WIMP response function.

transferred momentum, respectively. Therefore, the SD interacting coupling are $\mathcal{O}_3$, $\mathcal{O}_4$, $\mathcal{O}_6$, $\mathcal{O}_7$, $\mathcal{O}_9$, $\mathcal{O}_{10}$, $\mathcal{O}_{12}$, $\mathcal{O}_{13}$, $\mathcal{O}_{14}$ and $\mathcal{O}_{15}$. However, due to the fact that the velocity–dependent term in Eq(II.53) has less sensitive by $\left(\vec{v}^{\perp}\right)^2 \sim 10^{-3}$, for couplings $\mathcal{O}_i$ with i=3, 12, 13 and 15 are velocity–suppressed, while the dominant velocity–independent term couples to another nuclear response function. This implies that the truly "spin–dependent" couplings are only $\mathcal{O}_i$ with i=4, 6, 7, 9, 10 and 14.

According to the velocity dependence term in Eq(II.53), WIMP velocities are expected to be of order 10^{-3} in any velocity distribution, so in line 4 of Table(III.2) the velocity–dependent term is negligible. However, in line 8, the coupling term $\bar{\chi} i\sigma_{\mu\nu}\frac{q^\nu}{m_M}\gamma_5\chi\bar{N}\gamma_\mu\gamma_5 N$ leads to a velocity–suppressed cross section $\propto (v_T^\perp)^2$ without the corresponding velocity–independent contribution. The same thing can be achieved by appropriate linear combinations of the operator $\bar{\chi}\gamma^\mu\chi\bar{N}\gamma_\mu\gamma^5 N$ either

	Relativistic EFT	Nonrelativistic limit	$\sum_i \mathcal{O}_i$	cross section scaling
1	$\bar{\chi}\gamma^\mu\gamma^5\chi\bar{N}\gamma_\mu\gamma^5 N$	$-4\vec{S}_\chi\cdot\vec{S}_N$	$-4\mathcal{O}_4$	$W^{\tau\tau'}_{\Sigma'\Sigma'}(q^2)+W^{\tau\tau'}_{\Sigma''}(q^2)$
2	$2\bar{\chi}\gamma^\mu\chi\bar{N}\gamma_\mu\gamma^5 N+$ $+\bar{\chi}\gamma^\mu\gamma_5\chi\bar{N}i\sigma_{\mu\nu}\frac{q^\nu}{m_N}N$	$-4\vec{S}_N\cdot\vec{v}^\perp_T$	$-4\mathcal{O}_7$	$(v^\perp_T)^2 W^{\tau\tau'}_{\Sigma'}(q^2)$
3	$2\bar{\chi}\gamma^\mu\chi\bar{N}\gamma_\mu\gamma^5 N+$ $-\bar{\chi}i\sigma_{\mu\nu}\frac{q^\nu}{m_\chi}\chi\bar{N}\gamma^\mu\gamma_5 N$	$-4\vec{S}_N\cdot\vec{v}^\perp_T$	$-4\mathcal{O}_7$	$(v^\perp_T)^2 W^{\tau\tau'}_{\Sigma'}(q^2)$
4	$\bar{\chi}\gamma^\mu\chi\bar{N}\gamma_\mu\gamma^5 N$	$-2\vec{S}_N\cdot\vec{v}^\perp_T+$ $+\frac{2}{m_\chi}i\vec{S}_\chi\cdot\left(\vec{S}_N\times\vec{q}\right)$	$-2\mathcal{O}_7+2\frac{m_N}{m_\chi}\mathcal{O}_9$ $\simeq 2\frac{m_N}{m_\chi}\mathcal{O}_9$	$\simeq q^2 W^{\tau\tau'}_{\Sigma'}(q^2)$
5	$\bar{\chi}i\sigma_{\mu\nu}\frac{q^\nu}{m_M}\chi\bar{N}\gamma^\mu\gamma_5 N$	$4i(\frac{\vec{q}}{m_M}\times\vec{S}_\chi)\cdot\vec{S}_N$	$4\frac{m_N}{m_M}\mathcal{O}_9$	$q^2 W^{\tau\tau'}_{\Sigma'}(q^2)$
6	$\bar{\chi}\gamma^\mu\gamma_5\chi\bar{N}i\sigma_{\mu\nu}\frac{q^\nu}{m_M}N$	$4i\vec{S}_\chi\cdot(\frac{\vec{q}}{m_M}\times\vec{S}_N)$	$-4\frac{m_N}{m_M}\mathcal{O}_9$	$q^2 W^{\tau\tau'}_{\Sigma'}(q^2)$
7	$i\bar{\chi}\chi\bar{N}\gamma^5 N$	$i\frac{\vec{q}}{m_N}\cdot\vec{S}_N$	$\mathcal{O}_{10}$	$q^2 W^{\tau\tau'}_{\Sigma''}(q^2)$
8	$i\bar{\chi}i\sigma_{\mu\nu}\frac{q^\nu}{m_M}\gamma_5\chi\bar{N}\gamma_\mu\gamma_5 N$	$-4i(\frac{\vec{q}}{m_N}\cdot\vec{S}_\chi)(\vec{v}^\perp_T\cdot\vec{S}_N)$	$-4\frac{m_N}{m_M}\mathcal{O}_{14}$	$(v^\perp_T)^2 q^2 W^{\tau\tau'}_{\Sigma''}(q^2)$
9	$\bar{\chi}\gamma_5\chi\bar{N}\gamma^5 N$	$-\frac{\vec{q}}{m_\chi}\cdot\vec{S}_\chi\frac{\vec{q}}{m_N}\cdot\vec{S}_N$	$-\frac{m_N}{m_\chi}\mathcal{O}_6$	$q^4 W^{\tau\tau'}_{\Sigma''}(q^2)$
10	$\bar{\chi}i\sigma^{\mu\alpha}\frac{q_\alpha}{m_M}\gamma_5\chi\bar{N}i\sigma_{\mu\beta}\frac{q^\beta}{m_M}\gamma_5 N$	$4\frac{\vec{q}}{m_M}\cdot\vec{S}_\chi\frac{\vec{q}}{m_M}\cdot\vec{S}_N$	$4\frac{m_N^2}{m_M^2}\mathcal{O}_6$	$q^4 W^{\tau\tau'}_{\Sigma''}(q^2)$
11	$\bar{\chi}i\sigma^{\mu\nu}\frac{q_\nu}{m_M}\chi\bar{N}i\sigma_{\mu\alpha}\frac{q^\alpha}{m_M}N$	$4\left(\frac{\vec{q}}{m_M}\times\vec{S}_\chi\right)\cdot\left(\frac{\vec{q}}{m_M}\times\vec{S}_N\right)$	$4\left(\frac{q^2}{m_M^2}\mathcal{O}_4-\frac{m_N^2}{m_M^2}\mathcal{O}_6\right)$	$q^4 W^{\tau\tau'}_{\Sigma''}(q^2)$

Table III.2: Relativistic EFT for a Dark Matter fermionic WIMP χ having as a low–energy limit a generalized spin–dependent χ–nucleus elastic scattering. Some of the interaction terms in the second column contain an arbitrary scale m_M to ensure correct dimensionality.

with $\bar{\chi}\gamma^\mu\gamma_5\chi\bar{N}i\sigma_{\mu\nu}\frac{q^\nu}{m_\chi}N$ or $\bar{\chi}i\sigma_{\mu\nu}\frac{q^\nu}{m_\chi}\chi\bar{N}\gamma^\mu\gamma_5 N$, as shown in lines 2 and 3 of the same Table. In Table III.1 we ordered the models with powers of q^2: actually, as we will see in the following, the scaling with q^2 will be the most relevant property to interpret our numerical results.

With the exception of line 4 and line 11, all the models of Table III.2 correspond to one of the non–relativistic quantum–mechanical operators of Eq(II.49). This also holds for the model of line 4 that can be well approximated by $\mathcal{O}_9$. So in the following we will refer to each of these scenarios with the corresponding $\mathcal{O}_i$. On the other hand, the model of line 11 is given by a superposition of $\mathcal{O}_4$ and $\mathcal{O}_6$ with both contributions

of the same order. In Section (2) we will conventionally refer to this model as $\mathcal{O}_{46}$. In summary, we conclude that the most general spin–dependent models relevant from the point of view of the phenomenology of direct detection are seven: $\mathcal{O}_4$, $\mathcal{O}_7$, $\mathcal{O}_9$, $\mathcal{O}_{10}$, $\mathcal{O}_{14}$, $\mathcal{O}_6$, $\mathcal{O}_{46}$.

On the other hand, the given nuclear response functions from [64, 65, 66] is deficiency in targets(such as Chlorine). Therefore, we adopt usual SD interaction which is given in terms of the nuclear spin structure function[37] for c_4 coupling as :

$$S(q^2) = (c_4^0)^2 S_{00}(q^2) + c_4^0 c_4^1 S_{01}(q^2) + (c_4^1)^2 S_{11}(q^2). \tag{III.9}$$

Here the $S(q^2)$ is assumed as Gaussian form factor [90] :

$$\frac{S(q^2)}{S(0)} = e^{-q^2R^2/4}, \quad R = \left(0.92A_T^{1/3} + 2.68 - 0.78\sqrt{(A_T^{1/3}-3.8)^2+0.2}\right) \text{ fm}, \tag{III.10}$$

where the point like cross section is :

$$S(0) = \frac{1}{\pi}\frac{(2j_T+1)(j_T+1)}{j_T}\left(a_p\langle S_p\rangle + a_n\langle S_n\rangle\right)^2. \tag{III.11}$$

The identities for Eq(III.9), the WIMP response function, W, for Σ' and Σ'' can be

found as :

$$W_{\Sigma''}^{\tau\tau'}(q^2) = \frac{8}{3\pi}\frac{(2j_T+1)(j_T+1)}{j_T}\langle S^\tau\rangle\langle S^{\tau'}\rangle e^{-q^2R^2/4}$$
$$W_{\Sigma'}^{\tau\tau'}(q^2) = \frac{4}{3\pi}\frac{(2j_T+1)(j_T+1)}{j_T}\langle S^\tau\rangle\langle S^{\tau'}\rangle e^{-q^2R^2/4}, \qquad \text{(III.12)}$$

due to the fact that the Σ' and Σ'' can be assumed $W_{\Sigma'}^{\tau\tau'}(q^2) \simeq 2W_{\Sigma''}^{\tau\tau'}(q^2)$ when $q^2 \to 0$.

On the other hand, the velocity distribution corresponding decomposition in Eq(II.53) can be written as :

$$\tilde{\eta}(v_{\min}) = \frac{\rho_\chi \sigma_{ref}}{m_\chi}\int_{v_{\min}} d^3\vec{v}_T \frac{f(\vec{v}_T)}{v_T}, \qquad \text{(III.13)}$$
$$\tilde{\xi}(v_{\min}) = \frac{\rho_\chi \sigma_{ref}}{m_\chi}\int_{v_{\min}} d^3\vec{v}_T \frac{f(\vec{v}_T)}{v_T}\left(v_T^\perp\right)^2 = \int_{v_{\min}} d^3\vec{v}_T \frac{f(\vec{v}_T)}{v_T}\left(v_T^2 - v_{\min}^2\right).$$

(1) Compatibility factor

In this analysis, we focus the coupling constants for proton and neutron and m_χ. To find compatibility of experiments with the assumptions in Eq(III.3), quantitatively, it can be assessed introducing the following compatibility ratio [91] :

$$\mathcal{D}(m_\chi, c_n^i, c_p^i) \equiv \max_{i\in \text{signal}}\left(\frac{\bar{\tilde{\eta}}_i^{\text{DAMA-Na}} + \sigma_i}{\min_{j\le i}\bar{\tilde{\eta}}_{j,lim}}\right), \qquad \text{(III.14)}$$

where σ_i is the standard deviation of $\bar{\tilde{\eta}}_i^{\text{DAMA}}$ and $\bar{\tilde{\eta}}_{j,lim}$ is upper bound. The strategy of Eq(III.14) is that find the most constraining upper bound which violates decreasing assumption so the $\min_{j\le i}$ is required. For instance, when the $\mathcal{D} > 1$, one of the upper limits is constraint of DAMA, while the other case, all upper limits compatible with DAMA. On the other hand the bubble chambers and droplets cases, which are only sensitive to the threshold energy, such as SIMPLE, COUPP, PICASSO and PICO–2L, the strategy of to find expected event rate is quiet different with others due to the sensitivity. Since in this case it is not possible to map the corresponding bounds to arbitrary velocity bins. Notice that those experiment contain proton–odd targets so those have to be adopted in this analysis. In this experiments, i) we use the experimental DAMA modulation–amplitudes to get a conservative piecewise estimation $\tilde{\eta}_1^{est}(v_{\min})$ of the minimal $\tilde{\eta}_1$ modulated halo function compatible to the signal; ii) we obtain the corresponding estimation of the unmodulated part $\tilde{\eta}^{est}(v_{\min})$ by requiring that it is a decreasing function of $v_{\min}$ with $\tilde{\eta}^{est}(v_{\min}) \ge \tilde{\eta}_1^{est}(v_{\min})$; iii) in compliance with (III.3) and with the goal of obtaining a conservative bound, we require that the function $\tilde{\eta}$ is the *minimal* one able to explain the DAMA effect, so we assume $\tilde{\eta}^{est}(v_{\min} > v_2^{\text{DAMA,Na}})$=0; iv) we then use $\tilde{\eta}^{est}(v_{\min})$ to directly calculate for each experiment among k=SIMPLE, COUPP, PICASSO and PICO-2L and for each energy threshold $E_{th,i}$ the expected number of WIMP events $N_{k,i}^{expected}$ and compare it to the corresponding upper bound $N_{k,i}^{bound}$ (see section IIB. for further details). Then,

a straightforward generalization of the compatibility factor of Eq.(III.14) is:

$$\mathcal{D}(m_\chi, c_n^i/c_p^i) \to \max\left(\mathcal{D}(m_\chi, c_n^i/c_p^i), \frac{N_{k,i}^{expected}}{N_{k,i}^{bound}}\right). \qquad \text{(III.15)}$$

Notice that the above procedure is very general, since it allows to get a halo–independent bound in the case of any experiment that does not observe a signal. In particular this means that the requirement that one target dominates the expected rate is only needed to get estimations of the halo function from those experiments that observe an excess, but is not indispensable to get a conservative bound for those reporting a null result. In the following Section we will use the above definition of the compatibility factor to explore the WIMP parameter space for the generalized spin–dependent interactions introduced in Section II D.(3).

(2) Results

Each of the seven phenomenological models $\mathcal{O}_i$ (with i=4, 6, 7, 9, 10, 14, 46) listed at the end of Section II D.(3) depends on three parameters: the WIMP mass m_χ and the two components (c_i^p, c_i^n) of the corresponding effective coupling. However, following the halo–independent approach summarized in Section II D(1), we get our estimations of the $\tilde{\eta}$ or $\tilde{\xi}$ functions factorizing out the reference cross section $\sigma_{ref} = c_i^p \mu_{\chi N}/\pi$. As a consequence of this the coupling c_i^p cancels out in our definition (III.14,III.15)

of the compatibility factor $\mathcal{D}$. So in each model the phenomenology depends only on two parameters: m_χ and the ratio c_n^i/c_p^i (in the case of model $\mathcal{O}_{46}$ we factorize $\sigma_{ref} = c_6^p \mu_{\chi N}/\pi$).

Moreover, the models $\mathcal{O}_9$ and $\mathcal{O}_{14}$ only differ for an additional $(v_T^\perp)^2$ factor in the cross section, which is absorbed in the definition of the halo function $\tilde{\xi}$ (see Table III.2). The same is almost true for $\mathcal{O}_4$ and $\mathcal{O}_7$, apart from a different combination of the nuclear response functions, for which, however, $W_{\Sigma'}(q^2) \simeq 2W_{\Sigma''}(q^2)$ (at least for small q^2). So in the each pair the two models have identical or almost–identical compatibility factors $\mathcal{D}$ (in each case the estimations $\tilde{\xi}_i$ for the velocity–dependent model are simply rescaled by a common factor with respect to the corresponding $\tilde{\eta}_i$ in the velocity–independent one) . The bottom line is that only five relevant cases remain: $\mathcal{O}_4$, $\mathcal{O}_6$, $\mathcal{O}_9$, $\mathcal{O}_{10}$ and $\mathcal{O}_{46}$.

The results of our analysis is shown in Fig.III.12. The left–hand panel shows the contour plot in the m_χ– c_n^i/c_p^i plane for $\mathcal{D}$=1 of models $\mathcal{O}_i$, $i = 6, 46, 9, 10$ and a value close to the minimum ($\mathcal{D}$=1.7) for $\mathcal{O}_4$; the right–hand panel shows the minimum of $\mathcal{D}$ as a function of c_i^n/c_i^p at fixed m_χ plotted against m_χ. A few features arise from both plots: i) when $c^n/c^p \to$0 some intervals of m_χ exist where the DAMA effect is compatible to constraints from other direct–detection experiments for generalized spin–dependent interactions ($\mathcal{O}_i$, $i = 6, 46, 9, 10$), while the compatibility factor for the standard spin–dependent interaction $\mathcal{O}_4$ is always above $\mathcal{D}$=1; ii) from Table III.2

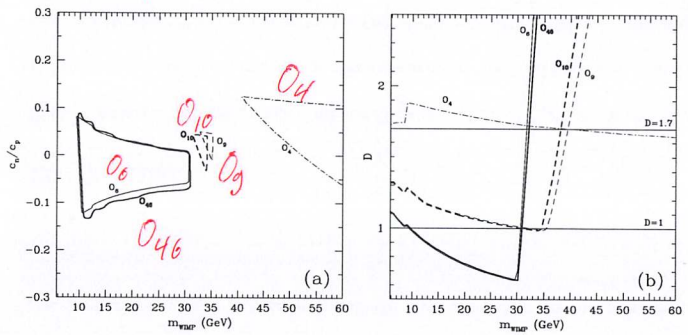

Figure III.12: **(a)** Contour plot in the m_χ–c_i^n/c_i^p plane for the compatibility factor $\mathcal{D}$ defined in Eqs. (III.14,III.15). The constant value $\mathcal{D}$=1 is shown for models $\mathcal{O}_i$, $i = 6, 46, 9, 10$, while a value close to the minimum ($\mathcal{D}$=1.7) is plotted for $\mathcal{O}_4$. **(b)** For the same models $\mathcal{O}_i$ the compatibility factor $\mathcal{D}$ is minimized as a function of c_i^n/c_i^p at fixed m_χ and plotted against m_χ.

one can see that the pairs of models $\mathcal{O}_6$–$\mathcal{O}_{46}$ and $\mathcal{O}_9$–$\mathcal{O}_{10}$ have the same momentum dependence, while they differ for the nuclear response function: since, however, as already pointed out $W_{\Sigma'}(q^2) \simeq 2W_{\Sigma''}(q^2)$ the compatibility factor $\mathcal{D}$ has very similar behaviours for the models in each pair ; ii) the tension between DAMA and other experiments is better alleviated in those models where momentum dependence is largest: in fact, models $\mathcal{O}_6$ and $\mathcal{O}_{46}$, which reach the best compatibility, depend on momentum through a factor q^4 compared to $\mathcal{O}_9$ and $\mathcal{O}_{10}$ where the dependence is through q^2 (see again Table III.2); iv) for $m_\chi \gtrsim 30$ GeV the compatibility factor rises steeply for models $\mathcal{O}_6$, $\mathcal{O}_{46}$, $\mathcal{O}_9$ and $\mathcal{O}_{10}$, while no such feature is observed for the case $\mathcal{O}_4$.

The last two properties can be understood in the following way. If $m_\chi \lesssim 30$ GeV, the WIMP signal in bubble chambers and droplet detectors is dominated by scatterings off fluorine. In particular, in this m_χ range in order to deposit recoil energies above threshold scatterings off iodine in COUPP require $v_{\rm min}$ values beyond the corresponding range for the DAMA signal, and we make the conservative assumption that in this case the halo function $\tilde{\eta}$ vanishes. Moreover scatterings off chlorine in SIMPLE are subdominant due to the suppressed nuclear response function. In this case the transferred momenta q^2 which explain the DAMA modulation effect for WIMP scatterings off sodium in DAMA are larger than the corresponding ones off fluorine in COUPP, PICASSO and PICO-2L. For instance, for m_χ=25 GeV

one has 285 MeV$^2 \lesssim (q^{\rm Na}_{\rm DAMA})^2 \lesssim$570 MeV^2, 275 MeV$^2 \lesssim (q^{\rm F}_{\rm COUPP})^2 \lesssim$470 MeV^2, 60 MeV$^2 \lesssim (q^{\rm F}_{\rm PICASSO})^2 \lesssim$470 MeV^2, 113 MeV$^2 \lesssim (q^{\rm F}_{\rm PICO-2L})^2 \lesssim$470 MeV^2. This implies that models where the expected detection rate depends on one additional factor $(q^2)^n$, $n > 0$ such as $\mathcal{O}_i$, $i = 6, 46, 9, 10$ present a relative enhancement of the expected rate in DAMA compared to that in fluorine detectors, with a consequent relative loss of sensitivity for the latter. An exception to this argument is SIMPLE, where the q^2 interval for scatterings off fluorine has more overlap with that of DAMA, 283 MeV$^2 < q^{\rm F}_{\rm SIMPLE} <$470 MeV^2, but which is overall less constraining than the other detectors due to the lower exposure. On the other hand, for $m_\chi \gtrsim$ 30 GeV scatterings off iodine in COUPP become kinematically allowed, with values of the transferred momenta which are much larger than those related to fluorine and sodium. For instance, for m_χ=35 GeV one has 1850 MeV$^2 \lesssim (q^{\rm I}_{\rm COUPP})^2 \lesssim$2350 MeV^2. Clearly, this implies a strong enhancement of the expected signal in COUPP for interactions involving an additional dependence on q^2, with a consequent steep rise of the compatibility factor $\mathcal{D}$, as observed in Fig. III.12. This effect is not present for the standard spin–dependent interaction $\mathcal{O}_4$, whose expected rate has no q^2 dependence.

In order to discuss in more detail the phenomenology in Figures III.13, III.14 and III.15 the measurements and bounds for the function $\tilde{\eta}$ obtained using Eq. (II.38) are plotted as a function of $v_{\rm min}$. In particular, in all these figures we take $c^i_n/c^i_p = 0$. Fig.

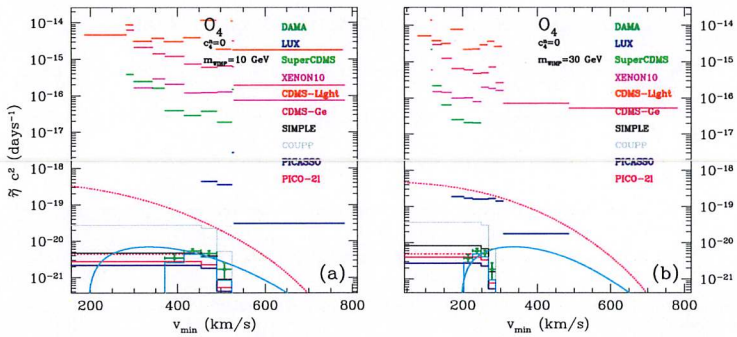

Figure III.13: Measurements and bounds for the function $\tilde{\eta}$ defined in Eq. (III.13) for model $\mathcal{O}_4$ (standard spin–dependent interaction) and c^n_4=0. **(a)** m_χ=10 GeV; **(b)** m_χ=30 GeV. The $\tilde{\xi}$ determinations for model $\mathcal{O}_7$ would be rescaled by an approximately common factor $\simeq 3/2$ with respect to the $\tilde{\eta}$ values shown in this figure.

III.13(a) shows the case of a standard spin–dependent interaction $\mathcal{O}_4$ when m_χ=10 GeV, while Fig. III.13(b) shows the same when m_χ=30 GeV. On the other hand, Figure III.14(a) shows the case of model $\mathcal{O}_6$ for m_χ=10 GeV while Fig. III.14(b) shows the same when m_χ=30 GeV. Finally, in Figure III.15(a) and III.15(b) model $\mathcal{O}_9$ is shown for m_χ=10 GeV and m_χ=33 GeV, respectively.

As discussed before, phenomenology of these models is practically degenerate with other scenarios. In particular, the $\tilde{\xi}$ determinations for model $\mathcal{O}_7$ would be rescaled by an approximately common factor ($\simeq 3/2$) with respect to the $\tilde{\eta}$ shown in figure III.13 for $\mathcal{O}_4$. In the same way the phenomenology of $\mathcal{O}_{46}$ is very similar to model $\mathcal{O}_6$, apart from an overall approximate factor ($\simeq 1/2$) in the $\tilde{\eta}$ determinations, so it can be described by Figure III.14. Moreover, the $\tilde{\xi}$ determinations for model $\mathcal{O}_{14}$ would be rescaled by an exact common factor of 2 with respect to the $\tilde{\eta}$ values shown in Figure III.15 for $\mathcal{O}_9$; on the other hand, the $\tilde{\eta}$ determinations for model $\mathcal{O}_{10}$ would be rescaled by an approximately common factor $\simeq 1/2$.

From all these plots we observe that germanium detectors and LUX can imply relatively lax constraints, due to the suppression of their nuclear response functions when c_i^n=0 (and, in the case of germanium, for the small natural abundance of ^{73}Ge, the only isotope carrying spin). Notice, however, that in the case of xenon and for interactions with an explicit momentum dependence the small residual contribution from protons to the spin can be enhanced by the q^n factor. For this reason in Figs.

III.14(b) and III.15(b) the LUX constraints on $\tilde{\eta}$ reach the level of DAMA, albeit at larger values of $v_{\rm min}$. This effect is maximal for $\mathcal{O}_6$ and $\mathcal{O}_{46}$ (with an explicit q^4 dependence in the cross section) and less severe for $\mathcal{O}_9$ and $\mathcal{O}_{14}$ (which depend on q^2) while is obviously absent for $\mathcal{O}_4$ and $\mathcal{O}_7$ which have no explicit momentum dependence.

In Figs. III.13, III.14 and III.15 the step–like cyan curve represents our conservative estimation $\tilde{\eta}_1^{est}(v_{\rm min})$ of the minimal $\tilde{\eta}_1$ modulated halo function compatible to the DAMA signal. In particular, as explained before, we assume that $\tilde{\eta}_1^{est}(v_{\rm min})$ vanishes outside the DAMA $v_{\rm min}$ interval. The corresponding estimation $\tilde{\eta}^{est}(v_{\rm min}) \geq \tilde{\eta}_1^{est}(v_{\rm min})$ of the minimal $\tilde{\eta}$ function is obtained by requiring it to be a decreasing function of $v_{\rm min}$ and is represented by the piecewise dotted red line.

As explained before, we use the function $\tilde{\eta}^{est}(v_{\rm min})$ to calculate the expected rate on droplet detectors and bubble chambers in the compatibility factor of Eq.(III.15). We decide to show the corresponding constraints by plotting for each experiment the function $\tilde{\eta}^{est}(v_{\rm min})$ rescaled by a constant factor in such a way that the corresponding expected rate is equal to the corresponding most constraining upper bound on the number of events. As can be seen from all the figures, also in the most favorable situations ($\mathcal{O}_6 \simeq \mathcal{O}_{46}$ for $m_\chi \simeq 30$ GeV) the bound is always relatively close (within one sigma) to the minimal DAMA signal. Since the DAMA estimations are for $\tilde{\eta}_1$ while the bounds are for $\tilde{\eta}$ this implies that compatibility among them necessarily requires a

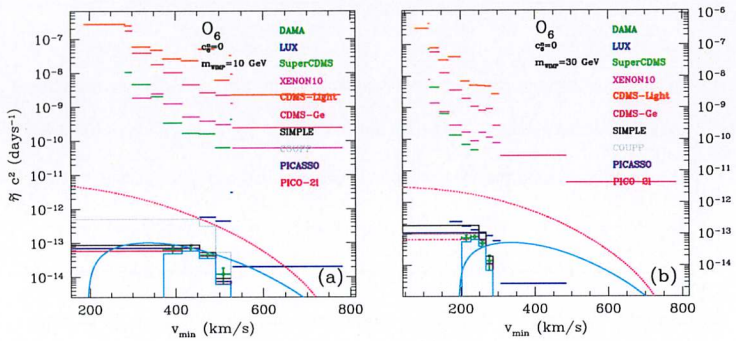

Figure III.14: The same as in Figure III.13 for model $\mathcal{O}_6$. The $\tilde{\eta}$ determinations for model $\mathcal{O}_{46}$ would be rescaled by an approximately common factor $\simeq 2$ with respect to the $\tilde{\eta}$ values shown in this figure.

modulation amplitude fraction in DAMA much larger then that predicted for a standard Isothermal Sphere (which is typically below 10%). In the same figures the continuous cyan line and dotted red line represent $\tilde{\eta}_1^{\rm Maxwellian}(v_{\rm min})$ and $\tilde{\eta}^{\rm Maxwellian}(v_{\rm min})$ for the case of a Maxwellian velocity distribution, where $\tilde{\eta}_1^{\rm Maxwellian}(v_{\rm min})$ is normalized in such a way to minimize a χ–square with the DAMA modulation amplitudes. Indeed, the red dotted line is well above existing constraints on $\tilde{\eta}$ in all cases. Moreover, notice that a Maxwellian for m_χ=30 GeV predicts a sizeable contribution to the event rate due to scatterings off iodine, so this explain the particularly poor fit with the $\tilde{\eta}$ estimations for DAMA, where dominance on sodium was assumed.

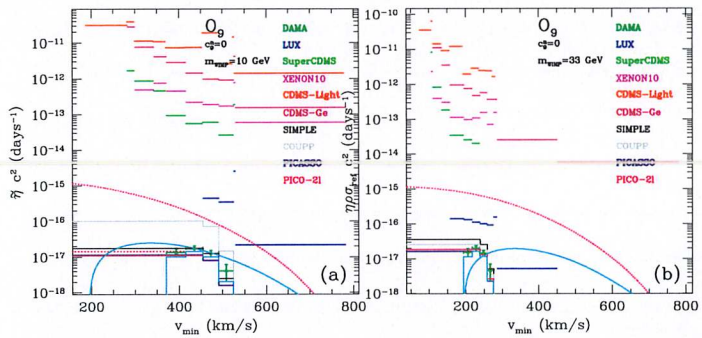

Figure III.15: The same as in Figure III.13 for model $\mathcal{O}_9$. The $\tilde{\xi}$ determinations for model $\mathcal{O}_{14}$ would be rescaled by a common factor 2 with respect to the $\tilde{\eta}$ values shown in this figure. The $\tilde{\eta}$ determinations for model $\mathcal{O}_{10}$ would be rescaled by an approximately common factor $\simeq 1/2$.

(3) Conclusions

In this section we have used non–relativistic Effective Field Theory to classify the most general spin–dependent WIMP–nucleus interactions, and within this class of models we have discussed the viability of an interpretation of the DAMA modulation result in terms of a WIMP signal, using a halo–independent approach in which all dependencies from astrophysics are factorized in a single halo function.

One of the main motivations of the spin–dependent scenario is the fact that the most stringent bounds on the interpretation of the DAMA effect in terms of WIMP–nuclei scatterings arise today from detectors using xenon (XENON100, LUX) and germanium (CDMS) whose spin is mostly originated by an unpaired neutron, while both sodium and iodine in DAMA have an unpaired proton: if the WIMP effective coupling to neutrons is suppressed compared to that on protons this class of bounds can be evaded. In this case the most constraining remaining bounds arise from droplet detectors (SIMPLE, COUPP) and bubble chambers (PICASSO, PICO-2L) , which all use nuclear targets (fluorine, chlorine and iodine) with an unpaired proton.

From the phenomenological point of view we found that, although several relativistic Effective Field Theories can lead to a spin–dependent cross section, in some cases involving an explicit dependence of the scattering cross section on the WIMP incoming velocity (see Table III.2), three main scenarios can be singled out in the

non–relativistic limit which (approximately) encompass them all, and that only differ by their explicit dependence on the transferred momentum, $(q^2)^n$, n=0,1,2: using the notation of Eq.(II.49), they are $\mathcal{O}_4$, $\mathcal{O}_9$ and $\mathcal{O}_6$, respectively.

In our quantitative analysis we pointed out that the requirement for a halo–independent analysis that one target dominates the expected rate is only needed to get estimations of the halo function from those experiments that observe an excess, but is not indispensable to get a conservative bound for those reporting a null result. We achieved this by adopting the procedure to find the minimal halo function $\tilde{\eta}^{est}(v_{\rm min})$ compatible to the DAMA signal and then use it to calculate expected rates in other experiments, including droplet detectors and bubble chambers which contain several target nuclei. Using this approach we also concluded that scatterings on iodine can be assumed to be below threshold in DAMA as long as $m_\chi \lesssim 60$ GeV, allowing the factorization of the halo function for sodium and evading the KIMS bound (also using iodine) in the same WIMP mass range.

In particular, we found that, for $m_\chi \lesssim 30$ GeV and with our assumptions on $\tilde{\eta}^{est}(v_{\rm min})$, the WIMP signal in bubble chambers and droplet detectors is dominated by scatterings off fluorine. In this case models where the expected detection rate depends on one additional factor $(q^2)^n$, $n > 0$ show a relative enhancement of the expected rate in DAMA compared to that in fluorine detectors, with a consequent relative loss of sensitivity for the latter, because the transferred momenta q^2 which

explain the DAMA modulation effect for WIMP scatterings off sodium are larger than the corresponding ones off fluorine. In this way compatibility between DAMA and other constraints can be achieved for $\mathcal{O}_6$ and, to a lesser extent, for $\mathcal{O}_9$, but not for the standard spin–dependent scenario $\mathcal{O}_4$. These conclusions are only valid for a WIMP velocity distribution in the halo of our Galaxy which departs from a Maxwellian. On the other hand, for $m_\chi \gtrsim 30$ GeV a strong tension between DAMA and COUPP arises for both $\mathcal{O}_6$ and $\mathcal{O}_9$ because scatterings off iodine in COUPP become kinematically allowed, with values of the transferred momenta which are much larger than those related to fluorine and sodium.

CHAPTER IV

CONCLUSION

When the standard approach in direct detection of WIMP is adopted the excesses from DAMA, CDMS–Si and CRESST are excluded by constraints from other experiments. However, assumptions such as a Maxwellian velocity distribution, spin–independent and spin–dependent interaction and elastic scattering, although well motivated are not confirmed by observations and may be wrong. Therefore, in this thesis we analyze i) spin–independent interaction within the halo–independent framework using inelastic dark matter and ii) elastic scattering of WIMPs with generalized spin–dependent interactions using non–relativistic effective field theory within the halo–independent framework. Moreover we also considered isospin violation where the WIMP particle has different couplings to protons and neutrons.

Our first result, explained in III A., is that, when the inelastic dark matter scenario is considered, at low WIMP masses an explanation of the DAMA excess in terms of

WIMP–sodium scatterings as well as the excess measured by CDMS with a silicon target are compatible with other upper limits for the spin–dependent interaction. However, they are non compatible among themselves. On the other hand WIMP scattering off iodine in DAMA at larger masses is incompatible with KIMS. Moreover, heavy WIMP scatterings off sodium in DAMA, when a different quenching factor is assumed, are incompatible with CDMS–Si or both CDMS–Si and CDMS–Ge. In particular, we provided the first systematical analysis of the inelastic dark matter scenario in a halo–independent way.

Our second result, which is explained in III B., uses non–relativistic effective field theory to study generalized spin–dependent interactions within the halo–independent framework. In our result, generalized spin–dependent interactions give compatible regions in the m_χ and c_n/c_p space when the DAMA effect explained by WIMP–sodium scatterings is compare to droplet detectors(SIMPLE, COUPP) and bubble chambers(PICASSO, PICO–2L) which contain fluorine, chlorine and iodine. The latter are all sensitive to the WIMP couplings to the proton c_p. However this compatibility is only possible when a velocity distribution different from a Maxwellian is adopted.

In our research we proposed new strategies to study WIMP direct detection considering a parameter space which is much wider than in the standard approach. In this way we were able to draw different conclusions than in the standard case : for instance within our framework we found the DAMA effect or the CDMS–Si excess and CRESST excess are not exclude by other constraints.

BIBLIOGRAPHY

[1] K. G. Begeman, A. H. Broeils, and R. H. Sanders, *Extended rotation curves of spiral galaxies: Dark haloes and modified dynamics*, *Mon. Not. Roy. Astron. Soc.* **249** (1991) 523.

[2] R. Bernabei et al., *New results and perspectives of DAMA/LIBRA*, *EPJ Web Conf.* **71** (2014) 00011.

[3] G. J. Feldman and R. D. Cousins, *A Unified approach to the classical statistical analysis of small signals*, *Phys. Rev.* **D57** (1998) 3873–3889, [physics/9711021].

[4] **PICASSO** Collaboration, S. Archambault et al., *Constraints on Low-Mass WIMP Interactions on ^{19}F from PICASSO*, *Phys. Lett.* **B711** (2012) 153–161, [arXiv:1202.1240].

[5] C. R. Contaldi, H. Hoekstra, and A. Lewis, *Joint CMB and weak lensing analysis: physically motivated constraints on cosmological parameters*, *Phys. Rev. Lett.* **90** (2003) 221303, [astro-ph/0302435].

[6] **Planck** Collaboration, P. A. R. Ade et al., *Planck 2013 results. XVI. Cosmological parameters*, *Astron. Astrophys.* **571** (2014) A16, [arXiv:1303.5076].

[7] **WMAP** Collaboration, E. Komatsu et al., *Seven-Year Wilkinson Microwave Anisotropy Probe (WMAP) Observations: Cosmological Interpretation*, *Astrophys. J. Suppl.* **192** (2011) 18, [arXiv:1001.4538].

[8] F. Zwicky, *Die Rotverschiebung von extragalaktischen Nebeln*, *Helv. Phys. Acta* **6** (1933) 110–127.

[9] F. Zwicky, *On the Masses of Nebulae and of Clusters of Nebulae*, *Astrophys. J.* **86** (1937) 217–246.

[10] V. C. Rubin and W. K. Ford, Jr., *Rotation of the Andromeda Nebula from a Spectroscopic Survey of Emission Regions*, *Astrophys. J.* **159** (1970) 379–403.

[11] M. Milgrom, *A modification of the newtonian dynamics - implications for galaxy systems*, *apj* **270** (July, 1983) 384.

[12] R. Cowsik and J. McClelland, *An Upper Limit on the Neutrino Rest Mass*, *Phys. Rev. Lett.* **29** (1972) 669–670.

[13] B. W. Lee and S. Weinberg, *Cosmological Lower Bound on Heavy Neutrino Masses*, *Phys. Rev. Lett.* **39** (1977) 165–168.

[14] S. D. M. White, C. S. Frenk, and M. Davis, *Clustering in a neutrino-dominated universe*, *apjl* **274** (Nov., 1983) L1–L5.

[15] **IceCube** Collaboration, J. Ahrens et al., *Sensitivity of the IceCube detector to astrophysical sources of high energy muon neutrinos*, *Astropart. Phys.* **20** (2004) 507–532, [astro-ph/0305196].

[16] **ANTARES** Collaboration, E. Aslanides et al., *A deep sea telescope for high-energy neutrinos*, astro-ph/9907432.

[17] M. W. Goodman and E. Witten, *Detectability of Certain Dark Matter Candidates*, *Phys. Rev.* **D31** (1985) 3059.

[18] J. D. Lewin and P. F. Smith, *Review of mathematics, numerical factors, and corrections for dark matter experiments based on elastic nuclear recoil*, *Astropart. Phys.* **6** (1996) 87–112.

[19] G. R. Knapp, S. D. Tremaine, and J. E. Gunn, *The global properties of the Galaxy. I - The H I distribution outside the solar circle*, *aj* **83** (Dec., 1978) 1585–1593.

[20] F. J. Kerr and D. Lynden-Bell, *Review of galactic constants*, *mnras* **221** (Aug., 1986) 1023–1038.

[21] J. A. R. Caldwell and I. M. Coulson, *Milky Way rotation and the distance to the galactic center from Cepheid variables*, *aj* **93** (May, 1987) 1090–1105.

[22] A. K. Drukier, K. Freese, and D. N. Spergel, *Detecting Cold Dark Matter Candidates*, *Phys. Rev.* **D33** (1986) 3495–3508.

[23] K. V. Johnston, D. N. Spergel, and L. Hernquist, *The disruption of the sagittarius dwarf galaxy*, *apj* **451** (Oct., 1995) 598, [astro-ph/9502005].

[24] V. Belokurov et al., *An Orphan in the Field of Streams*, *Astrophys. J.* **658** (2007) 337–344, [astro-ph/0605705].

[25] V. Belokurov et al., *The Field of Streams: Sagittarius and its Siblings*, *Astrophys. J.* **642** (2006) L137–L140, [astro-ph/0605025].

[26] M. Kuhlen, M. Lisanti, and D. N. Spergel, *Direct Detection of Dark Matter Debris Flows*, *Phys. Rev.* **D86** (2012) 063505, [arXiv:1202.0007].

[27] M. Lisanti and D. N. Spergel, *Dark Matter Debris Flows in the Milky Way*, *Phys. Dark Univ.* **1** (2012) 155–161, [arXiv:1105.4166].

[28] J. Diemand, M. Kuhlen, P. Madau, M. Zemp, B. Moore, D. Potter, and J. Stadel, *Clumps and streams in the local dark matter distribution*, *Nature* **454** (2008) 735–738, [arXiv:0805.1244].

[29] J. Stadel, D. Potter, B. Moore, J. Diemand, P. Madau, M. Zemp, M. Kuhlen, and V. Quilis, *Quantifying the heart of darkness with GHALO - a*

multi-billion particle simulation of our galactic halo, *Mon. Not. Roy. Astron. Soc.* **398** (2009) L21–L25, [arXiv:0808.2981].

[30] L. Hernquist, *An analytical model for spherical galaxies and bulges*, *apj* **356** (June, 1990) 359–364.

[31] A. V. Kravtsov, A. A. Klypin, J. S. Bullock, and J. R. Primack, *The Cores of dark matter dominated galaxies: Theory versus observations*, *Astrophys. J.* **502** (1998) 48, [astro-ph/9708176].

[32] B. Moore, T. R. Quinn, F. Governato, J. Stadel, and G. Lake, *Cold collapse and the core catastrophe*, *Mon. Not. Roy. Astron. Soc.* **310** (1999) 1147–1152, [astro-ph/9903164].

[33] J. F. Navarro, C. S. Frenk, and S. D. M. White, *A Universal density profile from hierarchical clustering*, *Astrophys. J.* **490** (1997) 493–508, [astro-ph/9611107].

[34] L. Bergstrom, P. Ullio, and J. H. Buckley, *Observability of gamma-rays from dark matter neutralino annihilations in the Milky Way halo*, *Astropart. Phys.* **9** (1998) 137–162, [astro-ph/9712318].

[35] R. H. Helm, *Inelastic and Elastic Scattering of 187-Mev Electrons from Selected Even-Even Nuclei*, *Phys. Rev.* **104** (1956) 1466–1475.

[36] B. Hahn, D. G. Ravenhall, and R. Hofstadter, *High-Energy Electron Scattering and the Charge Distributions of Selected Nuclei*, *Phys. Rev.* **101** (1956) 1131–1142.

[37] J. Engel, S. Pittel, and P. Vogel, *Nuclear physics of dark matter detection*, *Int. J. Mod. Phys.* **E1** (1992) 1–37.

[38] V. A. Bednyakov and F. Simkovic, *Nuclear spin structure in dark matter search: The Zero momentum transfer limit*, *Phys. Part. Nucl.* **36** (2005) 131–152, [hep-ph/0406218]. [Fiz. Elem. Chast. Atom. Yadra36,257(2005)].

[39] H. S. Lee et al., *Search for Low-Mass Dark Matter with CsI(Tl) Crystal Detectors*, *Phys. Rev.* **D90** (2014), no. 5 052006, [arXiv:1404.3443].

[40] **XENON10** Collaboration, J. Angle et al., *A search for light dark matter in XENON10 data*, *Phys. Rev. Lett.* **107** (2011) 051301, [arXiv:1104.3088]. [Erratum: Phys. Rev. Lett.110,249901(2013)].

[41] **LUX** Collaboration, D. S. Akerib et al., *First results from the LUX dark matter experiment at the Sanford Underground Research Facility*, *Phys. Rev. Lett.* **112** (2014) 091303, [arXiv:1310.8214].

[42] A. Alessandrello et al., *The thermal detection efficiency for recoils induced by low-energy nuclear reactions, neutrinos or weakly interacting massive particles*, *Phys. Lett.* **B408** (1997) 465–468.

[43] E. Simon et al., *SICANE: A Detector array for the measurement of nuclear recoil quenching factors using a monoenergetic neutron beam*, *Nucl. Instrum. Meth.* **A507** (2003) 643–656, [astro-ph/0212491].

[44] R. Bernabei et al., *New limits on WIMP search with large-mass low-radioactivity NaI(Tl) set-up at Gran Sasso*, *Phys. Lett.* **B389** (1996) 757–766.

[45] K. Fushimi, H. Ejiri, H. Kinoshita, N. Kudomi, K. Kume, K. Nagata, H. Ohsumi, K. Okada, H. Sano, and J. Tanaka, *Application of a large-volume nai scintillator to search for dark matter*, *Phys. Rev. C* **47** (Feb, 1993) R425–R428.

[46] **DAMA** Collaboration, R. Bernabei et al., *The DAMA/LIBRA apparatus*, *Nucl. Instrum. Meth.* **A592** (2008) 297–315, [arXiv:0804.2738].

[47] P. Sorensen and C. E. Dahl, *Nuclear recoil energy scale in liquid xenon with application to the direct detection of dark matter*, *Phys. Rev.* **D83** (2011) 063501, [arXiv:1101.6080].

[48] J. Lindhard, V Nielsen, M. Scharff and P.V. Thomsen, *INTEGRAL EQUATIONS GOVERNING RADIATION EFFECTS*, *Mat. Fys. Medd. Dan. Vid. Selsk.* **33** (1963), no. 10.

[49] **XENON100** Collaboration, E. Aprile et al., *Likelihood Approach to the First Dark Matter Results from XENON100*, *Phys. Rev.* **D84** (2011) 052003, [arXiv:1103.0303].

[50] D. McKinsey and R. Gaitskell, *First science results from the lux dark matter experiment*, 2013.

[51] **XENON100** Collaboration, E. Aprile et al., *Dark Matter Results from 225 Live Days of XENON100 Data*, *Phys. Rev. Lett.* **109** (2012) 181301, [arXiv:1207.5988].

[52] **XENON100** Collaboration, E. Aprile et al., *Dark Matter Results from 100 Live Days of XENON100 Data*, *Phys. Rev. Lett.* **107** (2011) 131302, [arXiv:1104.2549].

[53] H. Park et al., *Neutron beam test of CsI crystal for dark matter search*, *Nucl. Instrum. Meth.* **A491** (2002) 460–469, [nucl-ex/0202014].

[54] C. E. Aalseth et al., *Search for an Annual Modulation in a P-type Point Contact Germanium Dark Matter Detector*, *Phys. Rev. Lett.* **107** (2011) 141301, [arXiv:1106.0650].

[55] **CoGeNT** Collaboration, C. E. Aalseth et al., *CoGeNT: A Search for Low-Mass Dark Matter using p-type Point Contact Germanium Detectors*, *Phys. Rev.* **D88** (2013) 012002, [arXiv:1208.5737].

[56] **CoGeNT** Collaboration, C. E. Aalseth et al., *Search for An Annual Modulation in Three Years of CoGeNT Dark Matter Detector Data*, arXiv:1401.3295.

[57] **CoGeNT** Collaboration, C. E. Aalseth et al., *Experimental constraints on a dark matter origin for the DAMA annual modulation effect*, *Phys. Rev. Lett.* **101** (2008) 251301, [arXiv:0807.0879]. [Erratum: Phys. Rev. Lett.102,109903(2009)].

[58] **CDMS** Collaboration, R. Agnese et al., *Silicon Detector Dark Matter Results from the Final Exposure of CDMS II*, *Phys. Rev. Lett.* **111** (2013), no. 25 251301, [arXiv:1304.4279].

[59] **CDMS** Collaboration, Z. Ahmed et al., *Analysis of the low-energy electron-recoil spectrum of the CDMS experiment*, *Phys. Rev.* **D81** (2010) 042002, [arXiv:0907.1438].

[60] **SuperCDMS** Collaboration, R. Agnese et al., *Search for Low-Mass Weakly Interacting Massive Particles with SuperCDMS*, *Phys. Rev. Lett.* **112** (2014), no. 24 241302, [arXiv:1402.7137].

[61] **CDMS-II** Collaboration, Z. Ahmed et al., *Results from a Low-Energy Analysis of the CDMS II Germanium Data*, *Phys. Rev. Lett.* **106** (2011) 131302, [arXiv:1011.2482].

[62] **SuperCDMS** Collaboration, R. Agnese et al., *Search for Low-Mass Weakly Interacting Massive Particles Using Voltage-Assisted Calorimetric Ionization Detection in the SuperCDMS Experiment*, *Phys. Rev. Lett.* **112** (2014), no. 4 041302, [arXiv:1309.3259].

[63] M. Felizardo et al., *Final Analysis and Results of the Phase II SIMPLE Dark Matter Search*, *Phys. Rev. Lett.* **108** (2012) 201302, [arXiv:1106.3014].

[64] A. L. Fitzpatrick, W. Haxton, E. Katz, N. Lubbers, and Y. Xu, *The Effective Field Theory of Dark Matter Direct Detection*, *JCAP* **1302** (2013) 004, [arXiv:1203.3542].

[65] N. Anand, A. L. Fitzpatrick, and W. C. Haxton, *Weakly interacting massive particle-nucleus elastic scattering response*, *Phys. Rev.* **C89** (2014), no. 6 065501, [arXiv:1308.6288].

[66] R. Catena and B. Schwabe, *Form factors for dark matter capture by the Sun in effective theories*, *JCAP* **1504** (2015), no. 04 042, [arXiv:1501.03729].

[67] G. Angloher et al., *Results from 730 kg days of the CRESST-II Dark Matter Search*, *Eur. Phys. J.* **C72** (2012) 1971, [arXiv:1109.0702].

[68] R. Strauss, *New results from the cresst experiment*, 2014.

[69] "Cresst."

[70] **COUPP** Collaboration, E. Behnke et al., *First Dark Matter Search Results from a 4-kg CF_3I Bubble Chamber Operated in a Deep Underground Site*, *Phys. Rev.* **D86** (2012), no. 5 052001, [arXiv:1204.3094]. [Erratum: Phys. Rev.D90,no.7,079902(2014)].

[71] **PICO** Collaboration, C. Amole et al., *Dark Matter Search Results from the PICO-2L C_3F_8 Bubble Chamber*, *Phys. Rev. Lett.* **114** (2015), no. 23 231302, [arXiv:1503.00008].

[72] N. Fornengo and S. Scopel, *Temporal distortion of annual modulation at low recoil energies*, *Phys. Lett.* **B576** (2003) 189–194, [hep-ph/0301132].

[73] S. Yellin, *Finding an upper limit in the presence of unknown background*, *Phys. Rev.* **D66** (2002) 032005, [physics/0203002].

[74] D. Tucker-Smith and N. Weiner, *Inelastic dark matter*, *Phys. Rev.* **D64** (2001) 043502, [hep-ph/0101138].

[75] P. W. Graham, R. Harnik, S. Rajendran, and P. Saraswat, *Exothermic Dark Matter*, *Phys. Rev.* **D82** (2010) 063512, [arXiv:1004.0937].

[76] P. J. Fox, J. Liu, and N. Weiner, *Integrating Out Astrophysical Uncertainties*, *Phys. Rev.* **D83** (2011) 103514, [arXiv:1011.1915].

[77] P. Gondolo and G. B. Gelmini, *Halo independent comparison of direct dark matter detection data*, *JCAP* **1212** (2012) 015, [arXiv:1202.6359].

[78] E. Del Nobile, G. B. Gelmini, P. Gondolo, and J.-H. Huh, *Update on Light WIMP Limits: LUX, lite and Light*, *JCAP* **1403** (2014) 014, [arXiv:1311.4247].

[79] E. Del Nobile, G. B. Gelmini, P. Gondolo, and J.-H. Huh, *Halo-independent analysis of direct detection data for light WIMPs*, *JCAP* **1310** (2013) 026, [arXiv:1304.6183].

[80] M. T. Frandsen, F. Kahlhoefer, C. McCabe, S. Sarkar, and K. Schmidt-Hoberg, *Resolving astrophysical uncertainties in dark matter direct detection*, *JCAP* **1201** (2012) 024, [arXiv:1111.0292].

[81] S. Scopel, K.-H. Yoon, and J.-H. Yoon, *Generalized spin-dependent WIMP-nucleus interactions and the DAMA modulation effect*, *JCAP* **1507** (2015), no. 07 041, [arXiv:1505.01926].

[82] S. Chang, A. Pierce, and N. Weiner, *Momentum Dependent Dark Matter Scattering*, *JCAP* **1001** (2010) 006, [arXiv:0908.3192].

[83] S. Scopel and K. Yoon, *A systematic halo-independent analysis of direct detection data within the framework of Inelastic Dark Matter*, *JCAP* **1408** (2014) 060, [arXiv:1405.0364].

[84] N. Bozorgnia, J. Herrero-Garcia, T. Schwetz, and J. Zupan, *Halo-independent methods for inelastic dark matter scattering*, *JCAP* **1307** (2013) 049, [arXiv:1305.3575].

[85] J. Przyborowski and H. Wilenski, *Homogeneity of results in testing samples from poisson series*, *Biometrika* **31.3-4** (1940).

[86] J. L. Feng, J. Kumar, D. Marfatia, and D. Sanford, *Isospin-Violating Dark Matter*, *Phys. Lett.* **B703** (2011) 124–127, [arXiv:1102.4331].

[87] A. Kurylov and M. Kamionkowski, *Generalized analysis of weakly interacting massive particle searches*, *Phys. Rev.* **D69** (2004) 063503, [hep-ph/0307185].

[88] F. Giuliani, *Are direct search experiments sensitive to all spin-independent WIMP candidates?*, *Phys. Rev. Lett.* **95** (2005) 101301, [hep-ph/0504157].

[89] J. I. Collar, *Quenching and channeling of nuclear recoils in NaI(Tl): Implications for dark-matter searches*, *Phys. Rev.* **C88** (2013), no. 3 035806, [arXiv:1302.0796].

[90] G. Belanger, F. Boudjema, A. Pukhov, and A. Semenov, *Dark matter direct detection rate in a generic model with micrOMEGAs 2.2*, *Comput. Phys. Commun.* **180** (2009) 747–767, [arXiv:0803.2360].

[91] S. Scopel and J.-H. Yoon, *Effective scalar four-fermion interaction for Ge-phobic exothermic dark matter and the CDMS-II Silicon excess*, *Phys. Rev.* **D91** (2015), no. 1 015019, [arXiv:1411.3683].

- Use larger figure sizes.
  example: III 3 is too small
  III 15 is good

- Figures are clear but labels and legends can really improve them.